Numerical Modeling of a Midlatitude Squall Line: Features of the Convection and Vertical Momentum Flux

FRANK B. LIPPS* AND RICHARD S. HEMLER

Geophysical Fluid Dynamics Laboratory/NOAA, Princeton University, Princeton, New Jersey

(Manuscript received 26 June 1990, in final form 20 December 1990)

ABSTRACT

A 4-h simulation is carried out for the 22 May 1976 squall line that passed through the mesonetwork of the National Severe Storm Laboratory in central Oklahoma. This squall line was more than 100 km wide, oriented north–south and traveled eastward at approximately 14 m s^{-1}. It produced rainfall of 2-h duration at surface stations.

The simulation was obtained from a three-dimensional convective cloud model with open lateral boundary conditions on the east and west, and periodic conditions on the north and south boundaries. The model domain is 96 km long (east–west) and 32 km wide (north–south) with a horizontal grid resolution of 1.0 km and a vertical resolution of 0.5 km. A squall line develops and moves eastward at 13.7 m s^{-1} during the last two hours of the simulation. The present meso-γ-scale model, however, can only simulate the leading edge of the squall line, with rain at specific surface locations lasting only 30 min. Realistic features of the modeled flow include the surface westerlies moving faster than the line behind the gust front, the strong easterlies in the lower cloud levels, and the cold boundary layer behind the gust front.

Two-hour time means of the vertical momentum flux are calculated in a 60-km-wide domain (east–west) following the squall line. The vertical disturbance momentum flux for momentum normal to the line agrees with observations and is primarily confined to this region adjacent to the squall line. Horizontal-averaged time-mean momentum budgets are also calculated in this domain. For the normal component of momentum, this budget is in a quasi–steady state. It cannot be in a fully steady state as the gust front moves 1.2 m s^{-1} faster than the area of rain behind the line for the 2-h time mean.

The parameterization of Schneider and Lindzen for the vertical momentum flux associated with active clouds is compared with mean data from the simulation. Their parameterization accounts for the in-cloud vertical momentum flux reasonably well, but ignores the remaining flux associated with convective-scale downdrafts, which is significant in lower levels.

1. Introduction

A detailed observational analysis of the 22 May 1976 squall line in west-central Oklahoma was carried out by Ogura and Liou (1980). Their analysis revealed a north–south squall line more than 100 km wide that traveled eastward at approximately 14 m s^{-1}. Surface station data show a period of rainfall of approximately 2 h, and a sharp shift in the winds from southeast to northwest as the gust front passed. Time-mean north–south average vertical cross sections relative to the squall line are calculated for different physical variables. This observational study, as well as those to follow, made use of surface and radiosonde data collected from the National Severe Storms Laboratory mesonetwork, shown in Fig. 1 of Ogura and Liou (1980).

By also including radar and dual-Doppler radar data, Smull and Houze (1985, 1987a,b) are able to give a much more detailed analysis of the smaller-scale features associated with this line. Their results are summarized in the conceptual model shown in Fig. 1 of Smull and Houze (1987a). This model shows surface west winds (relative to the moving squall line) behind the surface gust front, easterly wind maxima in the lower cloud levels, and a long trailing anvil overlying a region of stratiform precipitation. A bright band of radar reflectivity at the freezing level is seen between 55 and 110 km behind the leading edge of the squall line. Smull and Houze (1987b) look at the role of rear inflow for this and other squall lines.

Two-dimensional simulations of this squall line have been carried out by Fovell and Ogura (1988). Using an idealized vertical sounding representing the air ahead of the line, they find a periodic time behavior for the rainfall intensity behind the leading edge. The width of the rainfall area is approximately 25 km for the rain-only simulation. For the simulation with the ice phase included, the width of the rainfall area is approximately 50 km, with progressively weaker rain-

---

* Dr. Frank B. Lipps died on 9 November 1990. This is one of several papers upon which he was working at the time of his death.

Corresponding author address: Mr. Richard Hemler, NOAA/ERL, Geophysical Fluid Dynamics Laboratory, Princeton University, Post Office Box 308, Princeton, NJ 08542.

fall intensity away from the leading edge. Thus, inclusion of the ice phase leads to a more realistic simulation with their model. The effect of varying the low-level vertical wind shear is discussed by Fovell and Ogura (1989).

The present investigation has two primary goals. The first is to determine how well both the small-scale and large-scale properties of this squall line can be simulated by a warm rain mesoγ-scale cloud model with horizontally homogeneous initial conditions and no large-scale forcing through either the lateral or lower boundaries. It was found that a long-lasting squall line did not develop in such a model unless cyclic boundary conditions were applied on the northern and southern boundaries, while maintaining open boundaries on the east and west. Such boundary conditions have been used in previous studies (Redelsperger and Lafore 1988; Rotunno et al. 1988; Yoshizaki and Ogura 1988) and provide a relatively easy means of generating a multicelled squall line without having to use detailed initial conditions and larger-scale forcing. In this study the strengths and weaknesses of such a model are assessed, through comparison of the latter stages of the model simulation with the available observational analyses of this squall line.

The second goal of the study is to compare the vertical flux of horizontal momentum in this simulation with observational data. There appears to be a growing consensus that two-dimensional models can simulate some basic properties of squall lines, such as longevity and strength, for lines in which weak to moderate shear is confined to the lower levels. This conclusion is stated in Weisman et al. (1988) and is referred to by Fovell and Ogura (1989). The present squall line environment has moderate shear confined primarily to lower levels, so that it appears to be included in this category. Indeed, Fovell and Ogura (1988) obtain many realistic features in their simulations. In a three-dimensional model, however, the horizontal air currents have the freedom to flow around isolated cells of deep convection, which they do not have in a two-dimensional model. This is considered to be an important physical effect for vertical momentum flux, especially at mid- to upper levels where the squall line flow becomes progressively more three-dimensional (Redelsperger and Lafore 1988). Therefore, in this study where vertical momentum flux is examined, a third dimension of modest width is included.

A detailed discussion of the moist convection model and the initial conditions for the study are given in section 2. In section 3 the model simulation is described and compared with available observations. Section 4 contains an analysis of the vertical momentum flux and momentum budgets. A comparison of the model momentum fluxes with the parameterization of Schneider and Lindzen (1976) is also given. Finally, in section 5, a discussion and evaluation of the results is presented.

2. The moist convection model

The basic properties of the numerical model are described in the tropical moist convection studies of Lipps and Hemler (1988, 1986) and the earlier scale analysis of Lipps and Hemler (1982). These studies are hereafter referred to as LH88, LH86, and LH82, respectively.

The convection is governed by a set of deep anelastic equations using Cartesian (x, y, z) coordinates. In these equations the atmospheric pressure p is represented through the Exner pressure function π, which is defined by

$$\pi = (p/P)^\kappa, \quad \kappa = R_d/c_p \qquad (2.1)$$

where P ($=1000$ mb) is a reference pressure, R_d ($=287.04$ J kg^{-1} K^{-1}) is the gas constant, and c_p ($=1005.7$ J kg^{-1} K^{-1}) is the specific heat at constant pressure for dry air.

The relation $T = \pi\theta$ between the temperature T and the potential temperature θ is obtained from the definition of θ. Following LH88 and LH82, the thermodynamic variables (θ, π, T) are separated into the base state components (θ_0, π_0, T_0) and the disturbance components (θ_1, π_1, T_1), which are associated with the convection.

The saturation water vapor mixing ratio q_{vs} is given by

$$q_{vs} = \frac{\epsilon e_s}{p_0 - e_s} \qquad (2.2)$$

where $p_0(z)$ is the base state pressure, e_s is the saturation vapor pressure, $\epsilon = R_d/R_v$, and R_v ($=461.50$ J kg^{-1} K^{-1}) is the gas constant for water vapor.

a. The equations of motion

1) CONTINUITY AND MOMENTUM

The equations of motion are written in tensor notation with the vector velocity (u, v, w) being denoted by u_i. For the anelastic set of equations (Ogura and Phillips 1962) continuity is represented by

$$\frac{\partial}{\partial x_j}(\rho_0 u_j) = 0 \qquad (2.3)$$

where $\rho_0(z)$ is the base state density.

The momentum equation in tensor form is given by

$$\frac{\partial}{\partial t}(\rho_0 u_i) + \frac{\partial}{\partial x_j}(\rho_0 u_i u_j) = -\rho_0 \frac{\partial \phi}{\partial x_i}$$
$$+ \delta_{i3}\rho_0 g \left(\frac{\theta_1}{\theta_0} + 0.608\, q_v - q_c - q_r\right) + \frac{\partial \tau_{ij}}{\partial x_j} \qquad (2.4)$$

where g ($=9.796$ m s^{-2}) is the acceleration due to gravity and τ_{ij} is the subgrid-scale Reynolds stress tensor. The present formulation of subgrid-scale turbu-

lence is discussed in the Appendix of LH88. The variable ϕ in (2.4) is defined as in LH82:

$$\phi = c_p \theta_0 \pi_1. \qquad (2.5)$$

The scale analysis indicates that ϕ is equal to the first-order pressure p_1 divided by the base state density ρ_0.

In the numerical solution of (2.4) the horizontal-averaged buoyancy term has been subtracted from this equation. Thus, denoting the buoyancy term by $\rho_0 g B$ and its horizontal average by $\rho_0 g \langle B \rangle$, Eq. (2.4) becomes

$$\frac{\partial}{\partial t}(\rho_0 u_i) + \frac{\partial}{\partial x_j}(\rho_0 u_i u_j)$$

$$= -\rho_0 \frac{\partial \phi_1}{\partial x_i} + \delta_{i3}\rho_0 g(B - \langle B \rangle) + \frac{\partial \tau_{ij}}{\partial x_j} \quad (2.4')$$

where $\phi_1 = \phi - \phi_{\langle B \rangle}$ and $\phi_{\langle B \rangle}$ is the component of ϕ that hydrostatically balances the horizontal-averaged buoyancy term $\rho_0 g \langle B \rangle$. Since the present equations are anelastic, ϕ_1 is calculated from a Poisson equation which is obtained from taking the divergence of (2.4').

2) THERMODYNAMICS AND MOISTURE

The thermodynamic equation is given by

$$\frac{\partial}{\partial t}(\rho_0 \theta_1) + \frac{\partial}{\partial x_j}[\rho_0 u_j(\theta_0 + \theta_1)]$$

$$= \frac{\rho_0 L}{c_p \pi_0}(C_d - E) - D_\theta - \frac{\partial}{\partial x_j}(\rho_0 \overline{u_j' \theta'}) \quad (2.6)$$

where $\rho_0 \overline{u_j' \theta'}$ are the subgrid-scale fluxes associated with θ. The form of $\rho_0 \overline{u_j' \theta'}$ as well as the corresponding moisture fluxes are given in the Appendix of LH88. Here C_d is the condensation–evaporation of cloud water q_c, E is the evaporation of rainwater q_r, and L ($=0.2501 \times 10^7$ J kg^{-1}) is the latent heat of vaporization at 0°C. This temperature in the base state occurs at $z = 3.5$ km and is located in the lower cloud levels in the model simulations. The values of C_d are determined by requiring $q_v \cong q_{vs}$ whenever cloud water q_c is present. The method for calculating C_d is given in appendix A of LH82.

In the present calculations, as in LH86 for deep tropical convection, spurious gravity waves tend to form near the upper boundary ($z = 17$ km) because of reflection and the strong static stability there. To eliminate this effect, the damping term $-D_\theta$ is included in (2.6) for $z > z_0$ with $z_0 = 11.25$ km and is given by

$$D_\theta = 10^{-5}(z - z_0)\rho_0(\theta_1 - \langle \theta_1 \rangle) \quad (2.7)$$

where the angle brackets indicate a horizontal average. With $z - z_0$ given in meters, (2.7) implies a damping time of 0.6 min at $z = 14$ km.

The present warm-rain bulk cloud physics follows Kessler (1969). Cloud water q_c moves with the air and

the rainwater q_r has the fall velocity $-V_T$ relative to the air. Thus, the equations governing moisture conservation are given by

$$\frac{\partial}{\partial t}(\rho_0 q_v) + \frac{\partial}{\partial x_j}(\rho_0 u_j q_v)$$

$$= -\rho_0(C_d - E) - \frac{\partial}{\partial x_j}(\rho_0 \overline{u_j' q_v'}) \quad (2.8)$$

$$\frac{\partial}{\partial t}(\rho_0 q_c) + \frac{\partial}{\partial x_j}(\rho_0 u_j q_c)$$

$$= \rho_0(C_d - S_a - S_c) - \frac{\partial}{\partial x_j}(\rho_0 \overline{u_j' q_c'}) \quad (2.9)$$

$$\frac{\partial}{\partial t}(\rho_0 q_r) + \frac{\partial}{\partial x_j}(\rho_0 u_j q_r) - \frac{\partial}{\partial z}(\rho_0 V_T q_r)$$

$$= \rho_0(S_a + S_c - E) - \frac{\partial}{\partial x_j}(\rho_0 \overline{u_j' q_r'}) \quad (2.10)$$

where S_a is the autoconversion of q_c into q_r, S_c is the collection of q_c by falling raindrops, and $\rho_0 \overline{u_j' q_v'}$, $\rho_0 \overline{u_j' q_c'}$, and $\rho_0 \overline{u_j' q_r'}$ are the subgrid-scale fluxes.

The bulk cloud physics used in this investigation follows that described in LH82. Thus, expressions for S_a, S_c, V_T, and E are given by Eqs. (A8)–(A11), respectively, from appendix A of LH82. We consider that this formulation is somewhat more appropriate for midlatitude continental convection than that given in LH86 and LH88, which was designed for warm-rain maritime convection.

b. Numerical methods

The numerical procedure for the present model follows that described in LH82 and LH88. Grid points for u, v, w, and ϕ_1 are staggered in space, with the Poisson equation for ϕ being solved at ϕ_1 grid points. The model domain is 96 km long (east–west), 32 km wide (north–south), and 17 km deep, with a horizontal grid resolution of 1.0 km and a vertical resolution of 0.5 km. A 10-s time step is used throughout the integration. In order to keep the primary cells within the model domain, the model coordinates were translated 9 m s^{-1} eastward and 4 m s^{-1} northward with respect to the earth's surface.

The momentum equation (2.4') is solved using centered space and time differences as discussed in LH82. The prognostic equations (2.8)–(2.10) for q_v, q_c, and q_r are solved using the modified Crowley scheme discussed by Clark (1979). This scheme eliminates the problem of numerically generated spurious negative values for these variables. The prognostic equation (2.6) for θ_1 is solved using the second-order Crowley scheme. This method of solution of (2.6) is consistent with the solution of the prognostic equation for q_v and allows an efficient numerical algorithm for calculating the condensation–evaporation C_d of cloud water.

c. Boundary conditions

1) LATERAL BOUNDARIES

Open lateral boundary conditions are applied on the western and eastern ends of the model while periodic conditions apply on the north and south. Specification is used at open inflow boundaries and extrapolation at open outflow boundaries for all prognostic variables but the normal velocities (Klemp and Wilhelmson 1978; Clark 1979).

A modified form of the Orlanski (1976) scheme is used to calculate normal velocities at open boundaries. For the u velocity at an x = constant boundary

$$\frac{\partial u}{\partial t} + c\frac{\partial u}{\partial x} = 0 \qquad (2.11)$$

where the phase velocity c is given by Eq. (2.1) of Orlanski (1976) and is constrained to lie in the range $0 \leq c \leq \Delta x/\Delta t$. In the Orlanski scheme, negative values of c obtained from his Eq. (2.1) are set equal to zero.

In some test calculations the present authors found that negative values of c often occurred when a local normal velocity extremum was located one grid point inside the boundary. Furthermore, setting c = 0 slowed the propagation of this feature out of the domain when compared with its rate of motion in a larger domain calculation. In order to speed the propagation of this type of feature out of the model domain, a modification has been made to the Orlanski scheme. When a local normal velocity extremum is located one grid point inside the boundary and the calculated value of c is negative, c is set equal to 30 m s^{-1}. This is a typical phase velocity for the fastest gravity wave in the domain (Klemp and Wilhelmson 1978).

The second modification of the Orlanski scheme is associated with the "runaway circulation" described by Clark (1979) as the computational excitation of a circulation composed of low-level inflow, upward motion, and upper-level outflow. To keep this circulation under control, Cho and Clark (1981) introduce a Rayleigh damping term at the inflow boundary

$$\frac{\partial u^*}{\partial t} = (1 - \epsilon)\frac{\partial u}{\partial t} + \epsilon(\bar{u}_{\pm\infty} - u^{\tau-1})/(2\Delta t) \quad (2.12)$$

where $\bar{u}_{\pm\infty}$ represents the environmental flow, $u^{\tau-1}$ is the flow at the boundary at the lag time step, $\partial u/\partial t$ is the tendency at the boundary without this adjustment, and

$$\left.\begin{array}{ll}\epsilon = 0.005 & \text{when } \bar{u}_{\pm\infty} \text{ is directed into the domain} \\ \epsilon = 0 & \text{when } \bar{u}_{\pm\infty} \text{ is directed out of the domain}\end{array}\right\}.$$
$$(2.13)$$

Inclusion of this adjustment results in a slow relaxation of the boundary flow to the environmental flow and tends to retard the runaway circulation. Note that this value of ϵ is one-fifth the magnitude of that used by

Cho and Clark, but is large enough to control the runaway circulation in the test calculations previously carried out.

2) VERTICAL BOUNDARIES

Rigid boundaries are assumed at the surface ($z = 0$) and model top ($z = 17$ km) so that $w = 0$ there. Due to the staggered grid, the variables u, v, θ, q_v, q_c, and q_r are evaluated at a one-half grid interval (0.25 km) from the upper boundary. At this level, the vertical gradients of the corresponding vertical subgrid-scale fluxes are required to vanish as in Klemp and Wilhelmson (1978). At the surface, vertical derivatives of q_c and q_r are required to vanish and a drag law formulation is used to specify $\rho_0 u'w'$, $\rho_0 v'w'$, $\rho_0 w'\theta'$, and $\rho_0 w'q_v'$. This formulation follows that given in LH86. For the simulation of continental convection, surface values of θ and q_v in the drag law formulation are set equal to the base state values of these variables shown in Fig. 1 at $z = 0$.
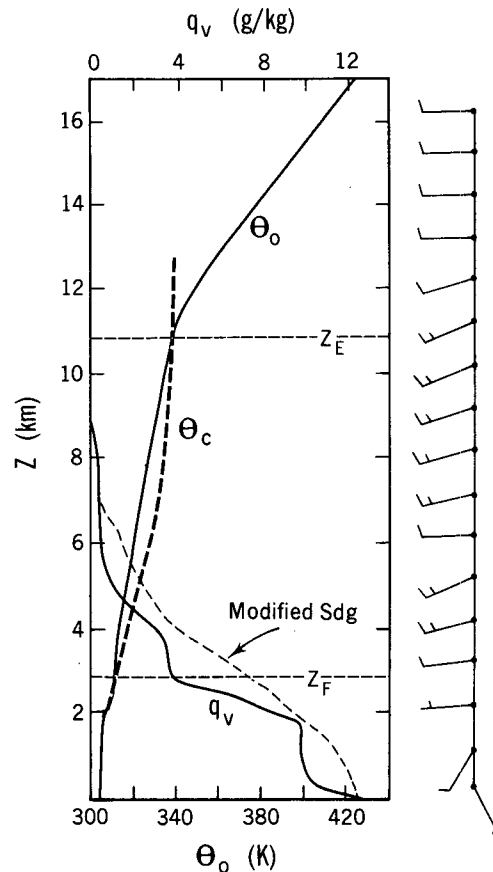

FIG. 1. Base state sounding for potential temperature θ_0, water vapor mixing ratio q_v, and wind with height. Full barb for wind is 10 m s^{-1}. Light-dashed curve represents moisture augmentation for the q_v sounding. Curve labeled θ_c represents a pseudomoist adiabatic sounding with the cloud base 1.8 km. Horizontal dashed lines are the level of free convection ($z = z_F$) and the equilibrium level ($z = z_E$).

d. Initial conditions

1) THE BASE STATE

The base state sounding for potential temperature θ_0, water vapor mixing ratio q_v, and wind as a function of z are shown in Fig. 1. Solid curves for θ_0 and q_v and the wind data were obtained from Fig. 2 of Ogura and Liou (1980, hereafter referred to as OL80) and represent the vertical sounding observed at Hinton, Oklahoma, at 1430 CST 22 May 1976. Note that the strong wind speed observed just above 200 mb has been smoothed in Fig. 1. It was thought that this localized upper-level jet would add unnecessary complexities to the simulation. Above 13 km the initial base state wind is taken as a constant velocity of 10 m s^{-1} from the west.

The light dashed curve in Fig. 1 indicates the effect of moisture augmentation and is more representative of the sounding just before the onset of convection. This profile for q_v was obtained using the relative humidity data shown at 1830 CST in Fig. 9 of OL80 as a guide. The moisture augmentation is an attempt to account for the lateral convergence of moisture that occurs as the squall line approaches, which the model does not take into account. Without this moisture augmentation, strong new cells do not continuously redevelop along outflow boundaries, and the squall line is short-lived. Similar modification to the initial temperature and wind fields have much less impact on the development of the squall line.

The heavy dashed line labeled θ_c in Fig. 1 was obtained from a pseudomoist adiabatic parcel calculation for which the lifting condensation level (LCL) at $z = 1.8$ km is taken as the cloud base. This calculation is carried out as described in Lipps and Hemler (1980). For this parcel calculation it is seen that the lowest cloud levels are stable, so that a weak cooling occurs in this region of negative buoyancy. The level of free convection (LFC) is at 2.8 km and the equilibrium level, which is the upper bound of the region of positive buoyancy, is at 10.8 km.

Various dynamical parameters have been calculated by Bluestein and Jain (1985) from the base state data for 40 different squall lines. When the mean over all 40 lines is taken, the mean dynamical properties are very similar to the values obtained from the present base state. The only significant exception is for the convective available potential energy (CAPE: Moncrieff and Miller 1976; Weisman and Klemp 1982). This parameter represents the net work per unit mass done by the environment on an in-cloud air parcel in the region of positive buoyancy:

$$\text{CAPE} = \int_{z_F}^{z_E} g\left(\frac{\theta_c - \theta_0}{\theta_0}\right) dz \qquad (2.14)$$

where the parcel has been lifted from the level of free convection (z_F) to the equilibrium level (z_E). For the

present base state CAPE = 1244 m^2 s^{-2}, whereas Bluestein and Jain found a mean value of 2260 m^2 s^{-2} and a standard deviation of 1100 m^2 s^{-2}. Thus, the value for the present base state is roughly one-half of the mean value obtained by Bluestein and Jain. This implies that the present sounding has relatively weak moist instability.

2) THE INITIAL DISTURBANCE

For the present model calculation the convection develops from an idealized initial disturbance for θ_1 and q_v. A bubble of warm saturated air exists in the region

$$\left.\begin{array}{c} -W \leqslant x - x_0 \leqslant W \\ -W \leqslant y - y_0 \leqslant W \\ -D_1 \leqslant z - z_0 \leqslant D_1 \end{array}\right\} \qquad (2.15)$$

where $W (=5$ km$)$ and $D_1 (=1.5$ km$)$ are the half-width and half-depth of the bubble. The coordinates (x_0, y_0, z_0) represent the center of the disturbance and are $(32.0, 16.0, 3.25)$ km, respectively, where $(0.0, 0.0, 0.0)$ is located at the surface in the southwest corner of the model domain. This disturbance is given by

$$\theta_1 = 0.75(1 - |z - z_0|/D_1)$$
$$\times \{1 - [(x - x_0)^2 + (y - y_0)^2]^{1/2}/W\} \qquad (2.16)$$
$$q_v = q_{vs} \qquad (2.17)$$

so that the maximum disturbance potential temperature is 0.75 K. There is no temperature disturbance below $z = 1.75$ km or above $z = 4.75$ km.

Above the saturated bubble, q_v is given by

$$q_v = q_{vs}\left[1 - 0.7\left(\frac{z - z_1}{D_2}\right)^2\right] \qquad (2.18)$$

where $z_1 = 4.75$ km and $D_2 = 7.0$ km. Thus, the relative humidity decreases with height, being 100% at 4.75 km and 30% at 11.75 km.

Due to the artificial nature of this initial disturbance, the first convective cell that forms is of limited physical interest. The emphasis in this investigation will instead be placed on the cells that develop in association with later gust front outflows.

3. Comparison of simulation and observations

a. General results

The plot of maximum vertical velocity versus time (Fig. 2) and the horizontal distribution of precipitation (Fig. 3) show the behavior of the convection during the 4-h simulation. The maximum vertical velocity (w_{max}) is seen to rise rapidly to a peak of just over 30 m s^{-1} at 20 min, in response to the initial forcing. A period of decay then follows with w_{max} reaching a minimum of less than 8 m s^{-1} at about 50 min. A rapid
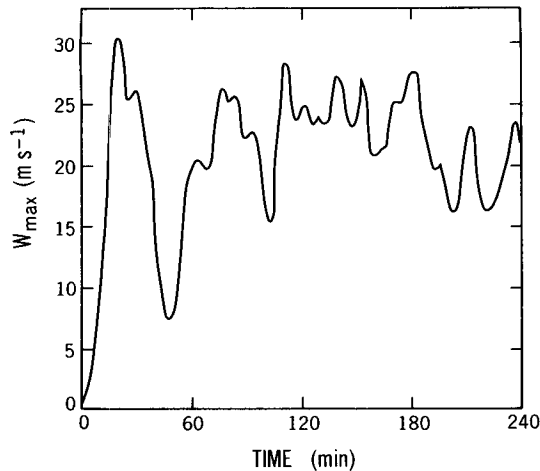
FIG. 2. Plot of w_{max} versus time for the simulation. A three-point time smoother has been applied to these data.

TABLE 1. Some characteristics of the convection and comparison with the observations of OL80. Levels of occurrence (z) are given in kilometers. See text for a definition of the characteristics listed.

	Simulation	Observation
w_{max} (m s^{-1})	28.6	ª
(z)	(8.0)	
θ'_{max} (K)	7.0	
(z)	(7.2)	
w_d (m s^{-1})	−7.2	
(z)	(1.5)	
w_g (m s^{-1})	8.7	
(z)	(1.5)	
U_g (m s^{-1})	14.9	18.7
U_R (m s^{-1})	13.7	13.9
$(\theta - \theta_0)_{sfc}$ (K)	−8.2	−11.1
$\langle R \rangle$ (cm)	0.39	
R_{max} (cm)	3.9	2.5

increase of w_{max} then follows, and for the remainder of the simulation, w_{max} is between 16 and 28 m s^{-1} with variations associated with the development and decay of individual cells.

The horizontal distribution of precipitation in Fig. 3 shows the presence of the many cells produced in the simulation. This horizontal section is for earth-fixed coordinates, not coordinates moving with the computational domain. In these coordinates, the center of the initial disturbance is located at $x = 4.6$ km and $y = 13.6$ km. Since the periodicity in y occurs over 32 km, the domain shown in Fig. 3 gives one repetition of the precipitation field in y. Precipitation from the initial cell is displaced from the initial disturbance location by the mean wind field shown in Fig. 1 and produces a precipitation maximum near $x = 27$ km and $y = 19$ km.

The second cell, located near $x = 40$ km and $y = 12$ km, forms to the southeast of the initial cell due to the convergence of gust fronts from the initial cell. One gust front travels southeastward from the initial cell

and the second approaches it across the periodic boundary at $y = 0$. As time progresses, new cells continue to develop along gust front outflows. They also form due to convergence of gust fronts and from the merger of existing cells. Precipitation from all of these cells form the pattern of precipitation shown in Fig. 3. Note that precipitation does not abruptly stop falling east of $x = 154$ km; rather, this position marks the eastern edge of the line at 4 h. The continuous line of precipitation greater than 1 cm found between $x = 73$ km and $x = 113$ km falls between approximately 120 and 180 min after the start of the simulation. The heaviest precipitation farther east falls, for the most part, after 180 min. A more detailed discussion of the convection associated with this heavier precipitation is given in section 3b.

A comparison of the simulation with the observed data discussed by OL80 is given in Table 1. Because the cell produced by the initial disturbance may not be realistic, it has been excluded from the data in this table. Parameters shown include the maximum vertical
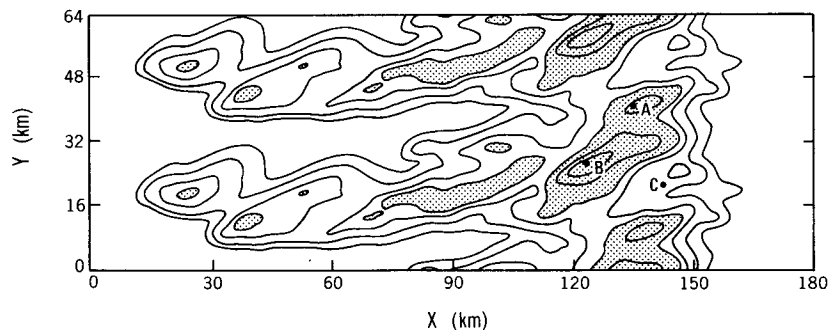

FIG. 3. Total accumulated precipitation at the ground during the 4-h simulation. Contours are plotted for 0.01, 0.1, 0.5, 1.0, 2.0, and 3.0 cm. Stippled areas represent precipitation in excess of 1.0 cm. Points A, B, and C are discussed in the text.

velocity w_{max}, the maximum disturbance potential temperature θ'_{max}, the maximum downdraft w_d, the maximum upward vertical velocity w_g along the gust front, the propagation speed U_g of the gust front, the propagation speed U_R of the leading edge of the rain at the ground, the coldest potential temperature ($\theta - \theta_0$)$_{sfc}$ at the surface, the horizontal-averaged accumulated precipitation $\langle R \rangle$ at the ground for the 180 km $\times$ 64 km area shown in Fig. 3, and the maximum precipitation R_{max} at a fixed point. Also shown in parentheses are the heights at which the extrema occurred. Note that the values of ($\theta - \theta_0$)$_{sfc}$ are taken from numerical data at $z = 0.25$ km.

Observed data are available in OL80 for U_g, U_R, ($\theta - \theta_0$)$_{sfc}$, and R_{max}. The value $U_g = 18.7$ m s^{-1} is the mean of the two observed propagation speeds of the gust front, (1) 20.2 m s^{-1} between CSM (Clinton-Sherman) and HNT (Hinton) and (2) 17.2 m s^{-1} between HNT and CHO (Choctaw). The value 13.9 m s^{-1} is equivalent to the propagation rate of 50 km h^{-1} of the squall line as measured by radar. The value ($\theta - \theta_0$)$_{sfc} = -11.1$ K is roughly equivalent to the temperature drop of 20°F seen in Fig. 7 of OL80 for CSM after the onset of heavy rain. Finally, $R_{max} = 2.5$ cm is obtained from the rainfall data given in the same figure for CSM.

These data show some interesting features of the simulation. The maximum values of w and θ' occur between 7 and 8 km. The value $\theta'_{max} = 7.0$ K is only slightly less than the maximum value of 7.5 K allowed by parcel theory. The maximum downdraft of -7.2 m s^{-1} at 1.5 km above the ground is associated with strong evaporative cooling in the falling rain. This vertical level is the same as that of the gust-front–induced vertical velocity maximum of 8.7 m s^{-1}. The average depth of rain over the entire 180 km $\times$ 64 km surface area in Fig. 3a is 0.39 cm. The values of U_g, U_R, and ($\theta - \theta_0$)$_{sfc}$ are slightly smaller than the observed values, perhaps due to the lack of the ice phase in the present cloud physics. The maximum rainfall $R_{max} = 3.9$ cm falls at point B labeled in Fig. 3. This value is larger than the 2.5 cm observed to fall at CSM in the observations. The fact that the value R_{max} is larger at point B than in the observations may be due to the moisture augmentation applied to the base state. It is also likely that the largest rainfalls occurring in the 22 May 1976 squall line were not recorded in the limited surface data presented in OL80.

b. Surface features of the simulation

Some features of the convection near the surface are shown at 210 min in Fig. 4. The pattern of vertical velocity in Fig. 4a at $z = 0.5$ km indicates clearly the line structure of the convection with the narrow width of the strong vertical velocity forced by the gust front outflows. Downward motion is found behind this leading edge of the convection where large values of rain-

water and positive pressure anomalies are present. These latter fields are plotted in Figs. 4b and 4c at $z = 0.25$ km, which is the level nearest the surface for the present staggered grid. The maximum pressure
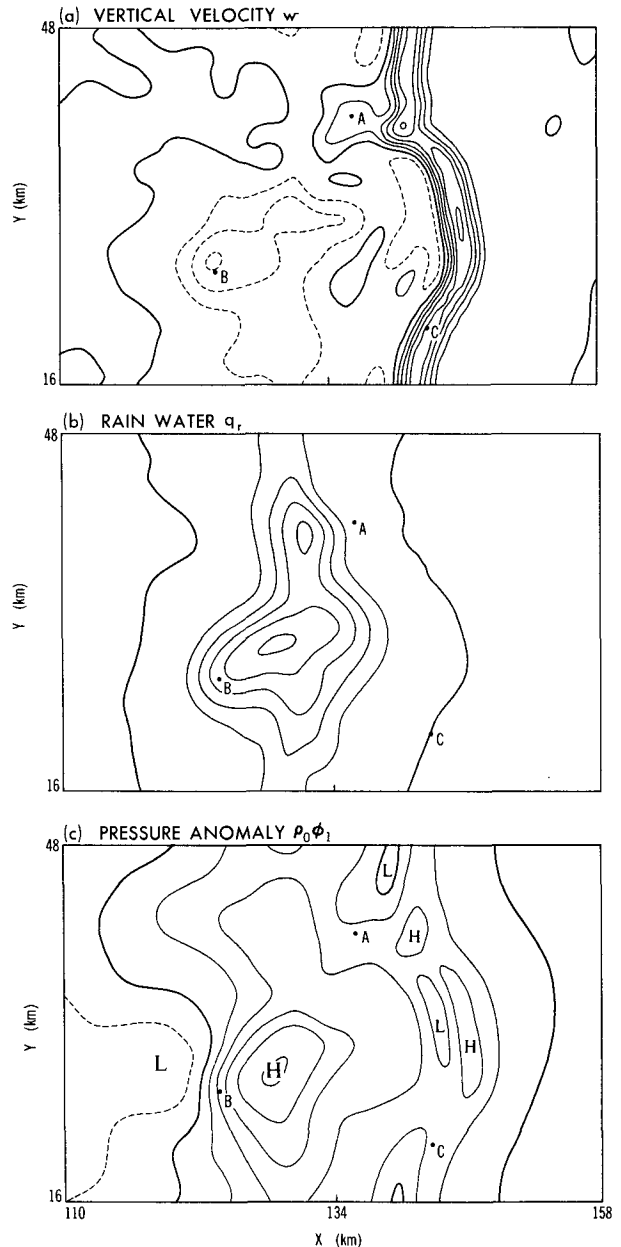

FIG. 4. Flow fields near the surface at 210 min. Negative values are indicated by dashed contours and the zero contour by the heavy line. (a) Vertical velocity w at $z = 0.5$ km with contour interval CI $= 1.0$ m s^{-1}, (b) rainwater q_r at $z = 0.25$ km with CI $= 0.75$ g kg^{-1}, and (c) pressure anomaly $\rho_0\phi_1$ at $z = 0.25$ km with CI $= 0.4$ mb. For (b) the heavy line represents $q_r = 0.01$ g kg^{-1}. In (c) large letters H and L represent the primary pressure anomalies. The small letters represent secondary centers. Maximum and minimum values of w, q_r, and $\rho_0\phi_1$ are, respectively, 5.2 and -3.1 m s^{-1}, 3.8 g kg^{-1}, 2.0 and -0.63 mb.

anomaly is 2 mb. The periodicity in y is evident on the northern and southern boundaries of the present figure.

Figures 3 and 4 have the same Cartesian coordinates and the points A, B, and C are at the same positions in both figures. The rainfall pattern in Fig. 3 indicates that A and B are in areas of large total rainfall, whereas C is in an area of light rain. In Fig. 4, A is behind the gust front and B is farther behind the gust front in the area with large values of rainwater, downdraft, and positive pressure anomaly. Point C is on the gust front at 210 min. The time variation of surface wind, pressure anomaly, rainfall, and potential temperature θ_1 at these three points is shown in Fig. 5. Note that θ_1 is zero before the squall line reaches these points. The form of Fig. 5 is similar to that of Fig. 7 in OL80.

The data in Fig. 5 indicate the heavy rainfall at points A and B, and the abrupt change of wind direction with the passing of the gust front at all three points. Furthermore, the maximum drop in potential temperature of 6–8 K after the passing of the gust front occurred at all three points. The total pressure rise seems correlated with total precipitation, with the largest pressure rise (2 mb) at point B. This pressure rise is one-half of that observed at CSM (4 mb). The data for the three points

(A, B, and C) indicate that, as in the observed squall line, the surface precipitation in the simulation varied markedly in space and time.

It is important to note that there are significant differences between the data in Fig. 5 and those shown in Fig. 7 of OL80. The width of the precipitation bars is 6 min in Fig. 5, but is 30 min for the data of OL80. Thus, the total time of rainfall was typically 30 min in this simulation, whereas for the observed line it was approximately two hours. In the simulation, the pressure rose just before or during the heavy rain as observed, but then immediately started falling. There was no extended period of high pressure such as observed at CSM and HNT. Hence, it appears that the present meso-γ-scale convection model simulates the leading edge of the squall line reasonably well but does not replicate the broad area of stratiform rain shown in Fig. 6 of OL80. As analyzed by Smull and Houze (1985), this rain is associated with the long trailing anvil and is clearly seen in the conceptual model of the 22 May 1976 squall line, as presented in Fig. 1 of Smull and Houze (1987a).

Another crucial difference between the present simulation and the observed data of OL80 is that the winds in Fig. 5 do not turn to the northwest behind the gust front. Since the vertical variation of wind in Fig. 1 (and in Fig. 2 of OL80 as well) does not show northwest winds above the ground, there is no dynamical reason to expect the winds in the present simulation to consistently shift to the northwest as observed. This deficiency will be discussed in more detail in section 5.

c. Vertical sections

Figure 6 shows various x–z cross sections at 210 min, which have been obtained by averaging in y across the full 32-km width of the computational domain. These y-averaged fields have been compared with cross sections at $y = 40.5$ km (not shown), which include point A shown in Figs. 3–5. The comparison of these two sets of cross sections indicates very similar features in the various fields. Thus, as suggested by the line structure of the convection shown in Fig. 4, the y-averaged fields give representative x–z cross sections, which can be compared with similar data in OL80 and with the conceptual model shown in Fig. 1 of Smull and Houze (1987a).

The field of y-averaged vertical velocity is shown in Fig. 6a. Strong upward motion is seen in the cloud, weaker downward motion is behind the cloud in the area of heavy rain, and a broad area of low-level upward motion is ahead of the main cloud and is associated with the gust front. As seen in Fig. 4a, the gust front has a bowed appearance along approximately one-half of its length in y. For this reason, the width of the area of low-level upward motion seen in Fig. 6a is broader than for an individual x–z cross section. The field of upward motion inside the cloud, however, has a similar
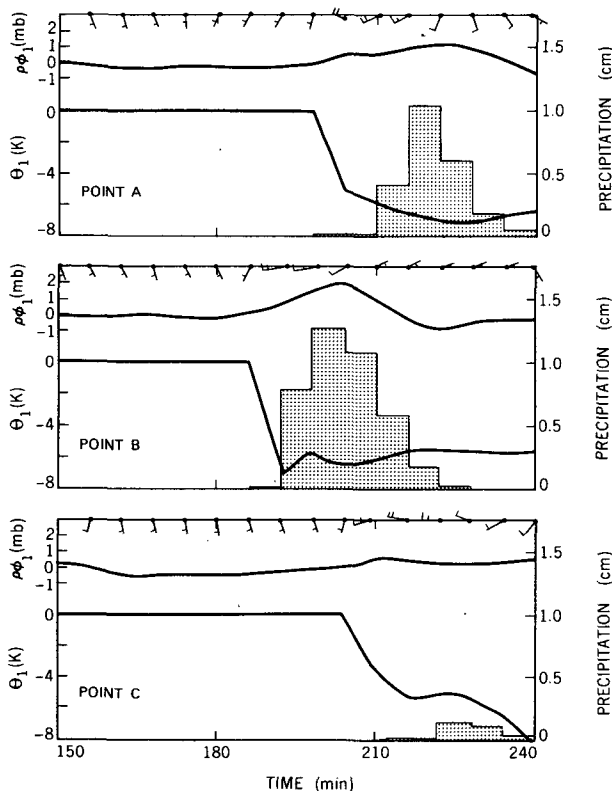

FIG. 5. Time variation of surface wind, pressure anomaly $\rho_0\phi_1$, potential temperature θ_1, and rainfall at points A, B, and C. Values for the wind, pressure anomaly, and potential temperature are taken from data at $z = 0.25$ km. Full barb for wind is 10 m s^{-1}.
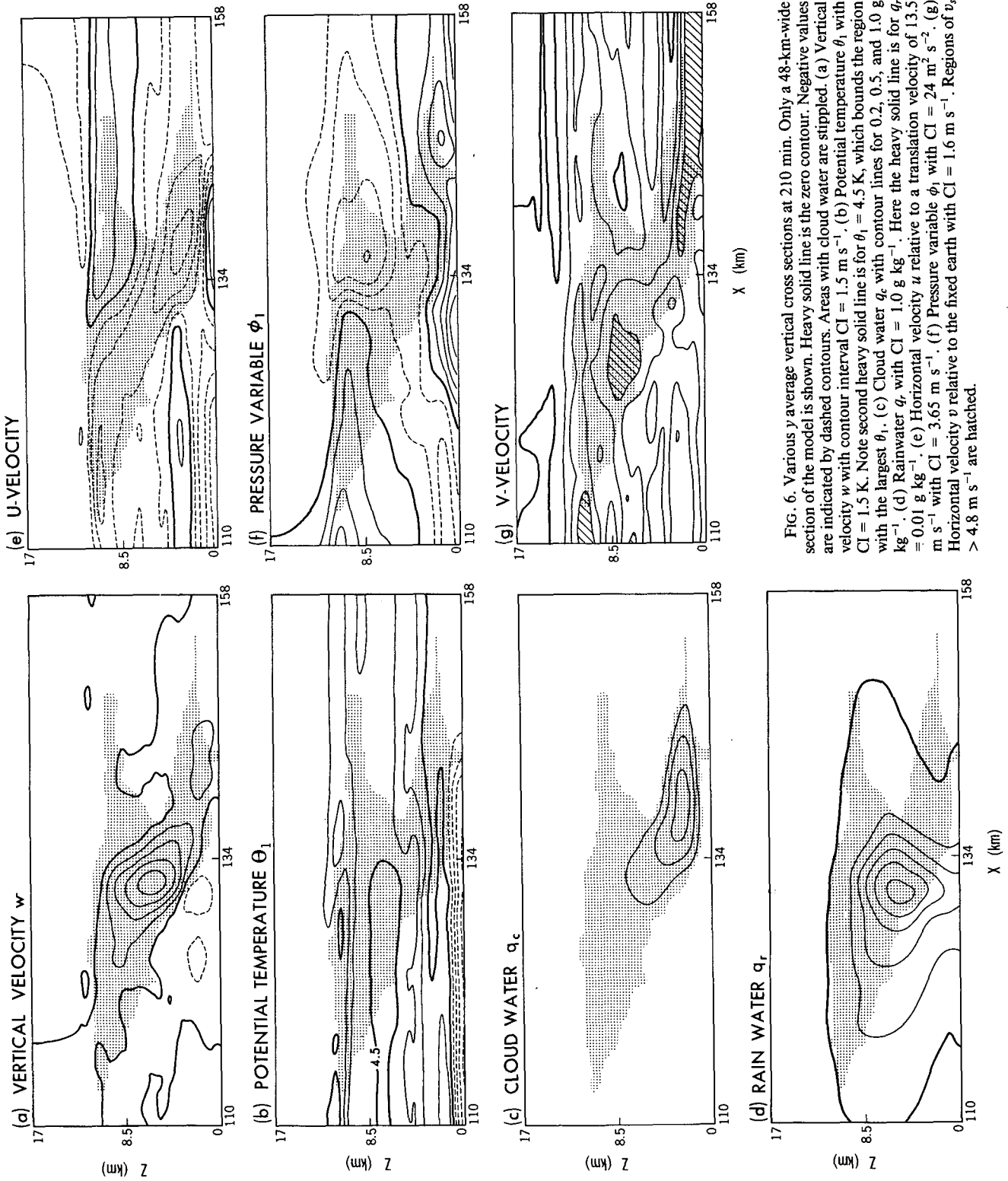
FIG. 6. Various y average vertical cross sections at 210 min. Only a 48-km-wide section of the model is shown. Heavy solid line is the zero contour. Negative values are indicated by dashed contours. Areas with cloud water are stippled. (a) Vertical velocity w with contour interval CI = 1.5 m s^{-1}. (b) Potential temperature θ_1 with CI = 1.5 K. Note second heavy solid line is for θ_1 = 4.5 K, which bounds the region with the largest θ_1. (c) Cloud water q_c with contour lines for 0.2, 0.5, and 1.0 g kg^{-1}. (d) Rainwater q_r with CI = 1.0 g kg^{-1}. Here the heavy solid line is for q_r = 0.01 g kg^{-1}. (e) Horizontal velocity u relative to a translation velocity of 13.5 m s^{-1} with CI = 3.65 m s^{-1}. (f) Pressure variable ϕ_1 with CI = 24 m^2 s^{-2}. (g) Horizontal velocity v relative to the fixed earth with CI = 1.6 m s^{-1}. Regions of v_s > 4.8 m s^{-1} are hatched.

spatial distribution to that found for the cross section at $y = 40.5$ km. In Fig. 6a, $w_{max} = 6.8$ m s^{-1} and $w_{min} = -2.6$ m s^{-1}. These values are roughly one-third as large as for the cross section at $y = 40.5$ km.

The field of potential temperature θ_1 is seen in Fig. 6b. Since $\theta_1 = 0$ at $t = 0$, this cross section shows the net effect of the convection on the potential temperature field over 20 min. The heavy solid contour for $\theta_1 = 4.5$ K bounds the region of the largest values of θ_1 near 7.5 km. The coldest values of potential temperature are found in the boundary layer behind the gust front. In this cross section, $(\theta_1)_{max} = 5.5$ K and $(\theta_1)_{min} = -6.5$ K. In the upper cloud levels, cooling is occurring above and upstream of the cloud due to evaporation and lifting of stable air. To the east of the main updraft, heating occurs due to subsidence. Another prominent feature is the thin layer of positive θ_1 just above the cold boundary layer. Largest values of θ_1 are near the western boundary, but positive θ_1 extends eastward, reaching the center of the main cloud. The dynamics associated with this feature are unclear.

The cross sections for cloud water q_c and rainwater q_r are shown in Figs. 6c and 6d. The stippled cloudy area indicates a relatively thick anvil to the rear and a thinner anvil to the east. Precipitation from the anvil extends about 30 km to the rear of the gust front, comparable to the rain area obtained by Fovell and Ogura (1988) in their no-ice simulation, but much less than the observed anvil rain extent of 110 km (Smull and Houze 1987a). Note that the rear anvil cloud is highly correlated with the upward motion field shown in Fig. 6a. Large values of cloud water in Fig. 6c are confined to lower layers, since at upper levels most of the cloud has been converted to rainwater.

The vertical x–z section for the u-velocity is given in Fig. 6e, where the velocity field shown is relative to a translation velocity 13.5 m s^{-1} toward the east. This translation speed is very close to the value of $U_R = 13.7$ m s^{-1} shown in Table 1 for this squall line. It is also the same translation velocity used by OL80. In Fig. 6e, a tendency toward conserving u inside the area of convection is seen, especially in mid- to upper levels. The flow pattern indicates easterlies in the boundary layer ahead of the line, maximum easterlies in the lower cloud levels, and a weak secondary maximum in the trailing anvil to the west as the air exits the cloud. The primary maximum in the easterlies occurs in the boundary layer outflow behind the line. In the conceptual model of Smull and Houze (1987a), the most prominent east wind feature is the maximum easterlies in the lower cloud levels.

A region of west wind outflow is seen in the upper levels to the east of the primary updraft. Another thin layer of west wind flow is present near 3 km to the west of the line. This feature brings some midlevel air from the west toward the line. The primary west wind feature, however, is the gust front outflow with a maximum velocity of 7.5 m s^{-1} at the surface. Note that

this is a smaller-scale feature than is resolvable in Fig. 13 of OL80. It is a prominent feature, however, in the conceptual model of Smull and Houze (1987a). Their model also shows a west wind outflow in the upper portion of the leading anvil.

The y-averaged pressure variable ϕ_1 is shown in Fig. 6f. The dominant feature of this ϕ_1-field is the high value at the surface behind the gust front in the region with downward velocity, evaporative cooling, and heavy water loading. In a qualitative way, the variations of u with x seen in Fig. 6e correspond with the $-\partial\phi_1/\partial x$ accelerations acting in the u momentum equation shown in this figure. For example, in mid- to upper cloud levels where u is most nearly conserved, the $-\partial\phi_1/\partial x$ accelerations are small. Likewise, in lower cloud levels where u is becoming increasingly negative, $-\partial\phi_1/\partial x$ is negative. Thus, the role of pressure accelerations in the lower cloud levels appears similar to that described by LeMone et al. (1984).

The vertical cross section for the v-velocity, relative to the fixed earth, is shown in Fig. 6g. Although there is some tendency for conservation of v inside the cloud, this effect is not as evident as for the u-velocity in Fig. 6e and it is much less evident than that seen in Fig. 14 of OL80. The vertical variation of v away from the cloud appears to be associated with the vertical variation of the base state v-field as shown in Figs. 1 and 8b. Although the southerly winds at the surface are weaker behind the gust front, there are no northerly winds at the surface, as are seen in Fig. 14 of OL80.

4. Analysis of vertical momentum flux

In this section the horizontal-averaged time-mean vertical momentum flux and the corresponding horizontal momentum budgets for the simulation are presented. Additionally, in section 4c, the parameterization of vertical momentum flux by Schneider and Lindzen (1976) is compared with the simulation data.

The analysis is carried out in a coordinate system moving with the squall line, translating eastward at 13.5 m s^{-1} with respect to the earth's surface. Northward velocity is calculated in earth-fixed coordinates, so that both velocities are consistent with the velocities plotted in Figs. 6e and 6g. Since these velocities are relative to the squall line they are denoted by u_s and v_s.

a. Vertical momentum flux

For the present analysis a horizontal average is taken over a subdomain moving with the squall line, extending 60 km in x and covering the full 32-km width of the model. A time mean is then applied to the horizontally averaged data from the final two hours of the simulation. Tensor notation is used so that $u_{si} = (u_s, v_s)$ represents the horizontal velocity.

In calculating the horizontal-averaged vertical mo-

mentum flux, the u_{si} and w velocities are separated into horizontal-averaged and deviation components

$$u_{si} = \langle u_{si} \rangle_s + u'_{si} \qquad (4.1a)$$

$$w = \langle w \rangle_s + w' \qquad (4.1b)$$

where the angle brackets with the subscript s denote the horizontal average following the squall line. Thus, the horizontal-averaged vertical momentum flux is given by

$$\rho_0 \langle u_{si} w \rangle_s = \rho_0 \langle u_{si} \rangle_s \langle w \rangle_s + \rho_0 \langle u'_{si} w' \rangle_s. \qquad (4.2)$$

Taking a time average for the last 2 h of the simulation gives

$$\rho_0 \overline{\langle u_{si} w \rangle_s} = \rho_0 \overline{\langle u_{si} \rangle_s \langle w \rangle_s} + \rho_0 \overline{\langle u'_{si} w' \rangle_s} \qquad (4.3)$$

where the bar represents the time average. In this equation, $\rho_0 \overline{\langle u_{si} w \rangle_s}$ is the total vertical momentum flux, $\rho_0 \overline{\langle u_{si} \rangle_s \langle w \rangle_s}$ is the mean flow vertical momentum flux, and $\rho_0 \overline{\langle u'_{si} w' \rangle_s}$ is the disturbance vertical momentum flux. For the present calculation, a good approximation to $\rho_0 \overline{\langle u_{si} \rangle_s \langle w \rangle_s}$ is given by

$$\rho_0 \overline{\langle u_{si} \rangle_s \langle w \rangle_s} \approx \rho_0 \overline{\langle u_{si} \rangle_s} \ \overline{\langle w \rangle_s}. \qquad (4.4)$$

A similar approximation will be made in applying the theory of Schneider and Lindzen (1976) to the present data.

The total vertical momentum fluxes $\rho_0 \overline{\langle u_s w \rangle_s}$ and $\rho_0 \overline{\langle v_s w \rangle_s}$ are shown by the solid curves in Fig. 7. As discussed earlier, the horizontal averages are taken in

a 60-km subdomain of the full 96-km domain in x. The dotted curves in Fig. 7 indicate similar total momentum fluxes, but averaged over the full 96-km domain and multiplied by a factor of eight-fifths. This horizontal average over the full domain is indicated by angle brackets without the subscript s. In comparing the solid and dotted curves in Fig. 7, it is noted that these curves would exactly overlie each other if the vertical momentum flux were zero everywhere outside of the 60-km subdomain following the squall line. In Fig. 7a the two curves are very similar; the curve for the full domain has slightly smaller values than the curve for $\rho_0 \overline{\langle u_s w \rangle_s}$ above $z = 4.0$ km and below $z = 1.5$ km. In Fig. 7b relatively larger differences are shown between the dotted curve and $\rho_0 \overline{\langle v_s w \rangle_s}$ for $z \geqslant 4.0$ km. Note, however, that due to the different scale in Fig. 7b, the actual magnitude of the difference between the two curves in Fig. 7b is similar to the corresponding difference between the two curves in Fig. 7a.

A primary conclusion from Fig. 7a is that the total vertical momentum flux $\rho_0 \langle u_s w \rangle$ over the full 96-km domain is mostly confined to the 60-km subdomain moving with the squall line. To a lesser degree, a similar conclusion can be inferred from Fig. 7b. The data in Fig. 7 also indicate that the values of $\rho_0 \overline{\langle v_s w \rangle_s}$ are at least a factor of four smaller than the largest value of $\rho_0 \overline{\langle u_s w \rangle_s}$. Note that the values of $\rho_0 \langle u_s w \rangle_s$ are negative for all z whereas the values of $\rho_0 \langle v_s w \rangle_s$ are positive, except for a very weak minimum located at 11 km.

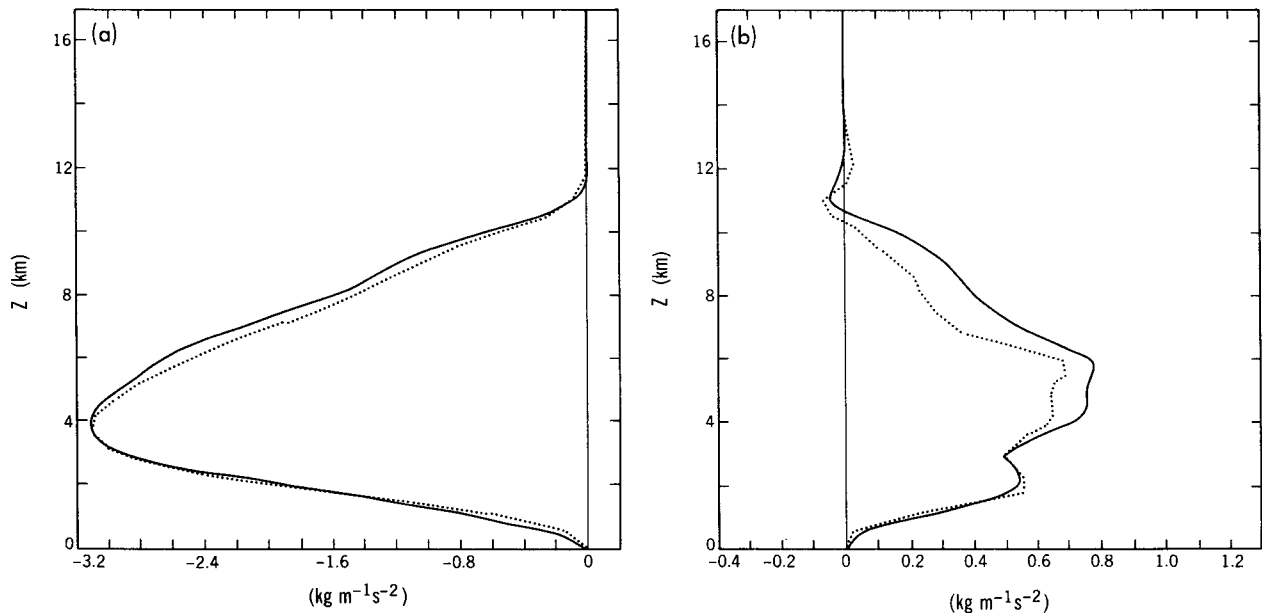In Fig. 8 the solid curves indicate the mean hori-

FIG. 7. (a) Total $\rho_0 \overline{\langle u_s w \rangle_s}$ for 60-km subdomain in x moving with the squall line (solid) versus $8/5$ $\rho_0 \overline{\langle u_s w \rangle}$ averaged over total domain (dotted). (b) Total $\rho_0 \overline{\langle v_s w \rangle_s}$ for the 60-km subdomain (solid) versus $8/5$ $\rho_0 \overline{\langle v_s w \rangle}$ averaged over total domain (dotted). Note difference in horizontal scale between (a) and (b).
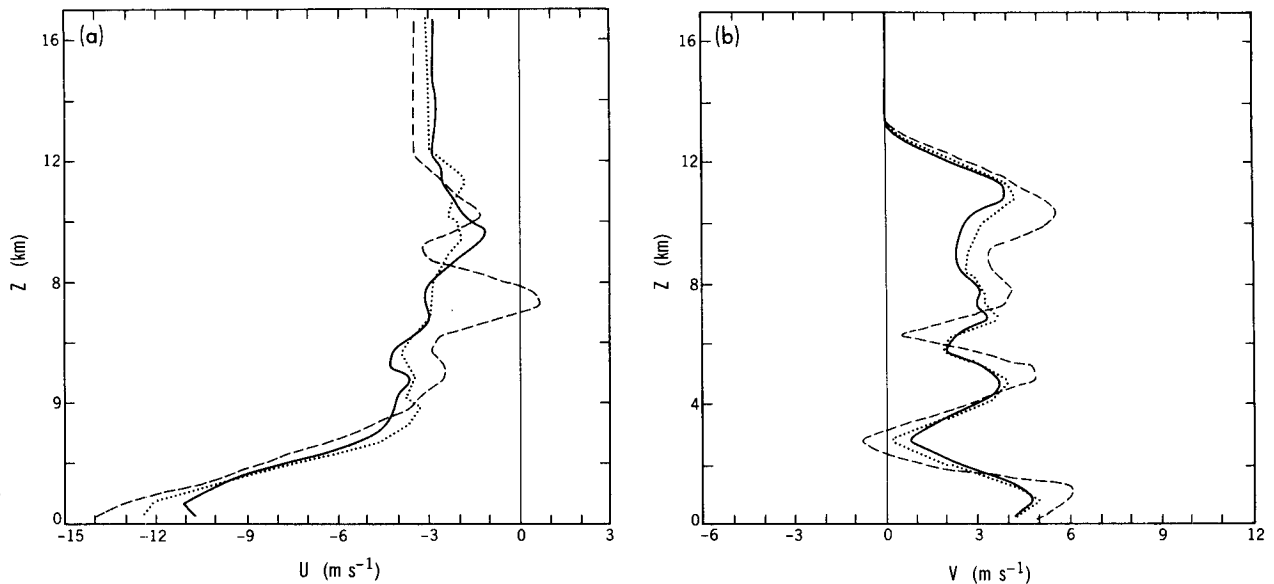
FIG. 8. (a) Time-mean horizontal average velocity $\overline{\langle u_s\rangle}_s$ following the squall line (solid), initial base state velocity u_0 (dashed), and time-mean horizontal-average velocity $\overline{\langle u_s\rangle}$ for the full 96-km domain (dotted curve). (b) Mean velocity $\overline{\langle v_s\rangle}_s$ following the squall line (solid), initial base state velocity v_0 (dashed), and mean velocity $\overline{\langle v_s\rangle}$ for the full 96-km domain (dotted curve).

zontal velocities $\overline{\langle u_s\rangle}_s$ and $\overline{\langle v_s\rangle}_s$ averaged following the squall line. The dotted curves represent the mean velocities $\overline{\langle u_s\rangle}$ and $\overline{\langle v_s\rangle}$ averaged over the full 96-km domain. Finally, the dashed curves indicate the initial base state velocities u_0 and v_0 obtained from Fig. 1. All velocity profiles start at $z = 0.25$ km, which is the first grid point above the ground for the present model.

The curves for $\overline{\langle u_s\rangle}_s$ and $\overline{\langle u_s\rangle}$ in Fig. 8a are in general much closer to each other than to the curve for u_0. A similar situation is also found in Fig. 8b where the curves for $\overline{\langle v_s\rangle}_s$, $\overline{\langle v_s\rangle}$, and v_0 are compared. Thus, the time-mean horizontal-averaged velocities are similar whether averaged following the squall line or averaged over the full horizontal domain. Somewhat of an exception to this rule is seen in Fig. 8a at $z = 0.25$ km where $\overline{\langle u_s\rangle}_s$ is 1.6 m s^{-1} less negative than $\overline{\langle u_s\rangle}$ and has a relative maximum at this level. This difference is apparently the result of the strong gust front outflow (seen in Fig. 6e at 210 min), which is a prominent feature in the 60-km domain following the squall line.

The total vertical momentum flux and its two components as given by (4.3) are plotted in Fig. 9. Values of total vertical momentum flux $\rho_0\langle u_s w\rangle_s$ (solid curve), disturbance vertical momentum flux $\rho_0\langle u_s' w'\rangle_s$ (dashed curve), and mean-flow vertical momentum flux $\rho_0\langle u_s\rangle_s\langle w\rangle_s$ (dotted curve) are shown in Fig. 9a. Corresponding curves for $\rho_0\langle v_s w\rangle_s$, $\rho_0\langle v_s' w'\rangle_s$, and $\rho_0\langle v_s\rangle_s\langle w\rangle_s$ are given in Fig. 9b. The present data in Fig. 9a can be compared with similar data shown in Fig. 12b of Lafore et al. (1988) obtained from the numerical simulation of an African squall line (23 June 1981). Both sets of curves

show similar vertical variation with height. The sign of the various momentum fluxes is opposite for the African case, as this squall line is in a region of strong low-level easterly wind shear and propagates westward with time. We note that the primary maximum in the curve for $\rho_0\langle u_s' w'\rangle_s$ is at 2 km for the African line, whereas it is at 3 km for the present case. This difference in dynamics is likely to be associated with the lower cloud base for the more moist African squall line.

The values of vertical momentum flux as shown in Fig. 12b of Lafore et al. (1988) are roughly a factor of four larger than seen in Fig. 9a. This difference can be explained in part due to the horizontal average being taken over a length of 30 km normal to the African squall line rather than over 60 km as done here. In this respect, the data in Fig. 6a suggest that the primary dynamics of the present squall line could also be represented by a 30-km-wide horizontal average. Taking this difference in averaging into account, the vertical mass flux associated with the African squall line, as shown in Fig. 11 of Lafore et al. (1988), appears to be twice as large as for the present case (not shown). The larger mass flux is consistent with the stronger convective instability of the African squall line. Chalon et al. (1988) find CAPE $= 2810$ for the 23 June 1981 squall line, whereas in the present case CAPE $= 1244$ as discussed in section 2d. Thus, considering both the method of horizontal averaging and the larger vertical mass flux for the African squall line, the two profile sets for vertical momentum flux appear to be consistent.

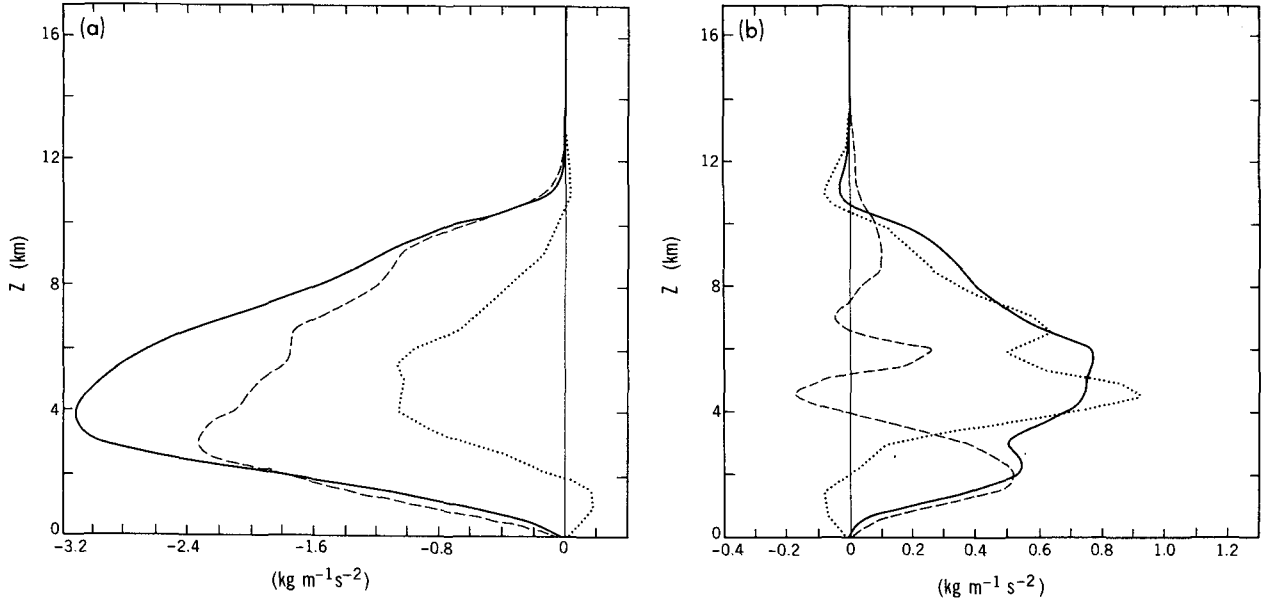The present analysis has been carried out with the positive x-axis in the direction of squall line motion.

FIG. 9. Different components of vertical momentum flux following the squall line as given by (4.3). (a) Total vertical momentum flux $\rho_0\langle\overline{u_s w}\rangle_s$ (solid line), disturbance vertical momentum flux $\rho_0\langle\overline{u_s' w'}\rangle_s$ (dashed line), and mean flow vertical momentum flux $\rho_0\langle\overline{u_s}\rangle_s\langle\overline{w}\rangle_s$ (dotted curve). (b) Total vertical momentum flux $\rho_0\overline{\langle v_s w\rangle}_s$ (solid line), disturbance vertical momentum flux $\rho_0\langle\overline{v_s' w'}\rangle_s$ (dashed line), and mean flow vertical momentum flux $\rho_0\langle\overline{v_s}\rangle_s\langle\overline{w}\rangle_s$ (dotted line).

This is the same convention as used by LeMone et al. (1984), who found from observed data

$$\rho_0\langle\overline{u_s' w'}\rangle_s < 0, \quad \rho_0\langle\overline{v_s' w'}\rangle_s \approx -\frac{\partial}{\partial z}\langle\overline{v_s}\rangle_s. \quad (4.5)$$

These relations are equivalent to their Eq. (3). Since the curve for $\rho_0\langle\overline{u_s' w'}\rangle_s$ in Fig. 9a is everywhere negative, the first of these two relations is clearly satisfied by the present data. The observed and simulated values of $\rho_0\langle\overline{u_s' w'}\rangle_s$ for the African squall line shown in Fig. 12 of Lafore et al. (1988) are also consistent with the first relation of (4.5) when it is remembered that their squall line propagates in the negative x-direction.

Comparing the curve for $\rho_0\langle\overline{v_s' w'}\rangle_s$ in Fig. 9b with the curve for $\langle\overline{v_s}\rangle_s$ in Fig. 8b, we find that the second relation of (4.5) is valid for the lower-level maximum in $\rho_0\langle\overline{v_s' w'}\rangle_s$. Above $z = 2.75$ km, however, it appears that the vertical gradient of $\rho_0\langle\overline{v_s' w'}\rangle_s$ is closely correlated with the negative vertical gradient of $\langle\overline{v_s}\rangle_s$. The present variation of $\rho_0\langle\overline{v_s' w'}\rangle_s$ at midlevels is consistent with the parameterization of Schneider and Lindzen (1976), as will be discussed in section 4c. Thus, we find that the present values of $\rho_0\langle\overline{u_s' w'}\rangle_s$ agree well with (4.5) for all z, whereas the values of $\rho_0\langle\overline{v_s' w'}\rangle_s$ agree well only for $z \leqslant 2.75$ km.

The data in Fig. 9 indicate that values of line-normal disturbance momentum flux $\rho_0\langle\overline{u_s' w'}\rangle_s$ are at least a factor of four larger than the values of alongline disturbance momentum flux $\rho_0\langle\overline{v_s' w'}\rangle_s$. Similar results are found for the African squall line (Lafore et al. 1988) and for fast moving tropical squall lines over the ocean

(LeMone et al. 1984). This difference may be due in part to the larger low-level vertical shear in $\langle\overline{u_s}\rangle_s$ compared with $\langle\overline{v_s}\rangle_s$. It is also likely to be due to the different dynamics involved with the $\rho_0\langle\overline{u_s' w'}\rangle_s$ and $\rho_0\langle\overline{v_s' w'}\rangle_s$ momentum flux budgets (LeMone 1983; LeMone et al. 1984).

According to the approximate relation (4.4), the values of $\rho_0\langle\overline{u_s}\rangle_s\langle\overline{w}\rangle_s$ and $\rho_0\langle\overline{v_s}\rangle_s\langle\overline{w}\rangle_s$ plotted in Fig. 9 are strongly dependent on the mean horizontal velocities $\langle\overline{u_s}\rangle_s$ and $\langle\overline{v_s}\rangle_s$ and on the mean vertical mass flux $\rho_0\langle\overline{w}\rangle_s$. For example, at $z = 5$ km we have $\langle\overline{u_s}\rangle_s = -3.9$ m s^{-1}, $\langle\overline{v_s}\rangle_s = 3.6$ m s^{-1}, and $\rho_0\langle\overline{w_s}\rangle_s = 0.25$ kg m^{-2} s^{-1}. Using (4.4) we find $\rho_0\langle\overline{u_s}\rangle_s\langle\overline{w}\rangle_s \approx -1.00$ kg m^{-1} s^{-2} and $\rho_0\langle\overline{v_s}\rangle_s\langle\overline{w}\rangle_s \approx 0.896$ kg m^{-1} s^{-2} at this level. These approximate values are very close to the values given at $z = 5$ km in Fig. 9. When the total vertical profiles are considered, it is seen that $\rho_0\langle\overline{u_s}\rangle_s\langle\overline{w}\rangle_s$ makes the smaller contribution to the total $\rho_0\langle\overline{u_s w}\rangle_s$ in Fig. 9a, whereas $\rho_0\langle\overline{v_s}\rangle_s\langle\overline{w}\rangle_s$ makes the dominant contribution to the total $\rho_0\langle\overline{v_s w}\rangle_s$ for $z \geqslant 3.5$ km in Fig. 9b.

b. Horizontal momentum budgets

The vertically varying horizontal momentum budgets for the zonal and meridional flow are given in the following. As in the previous discussion, the horizontal average is taken for the 60-km subdomain in x, which follows the squall line, and the time average is taken over the last two hours of the simulation. The horizontal momentum budget equations are obtained by
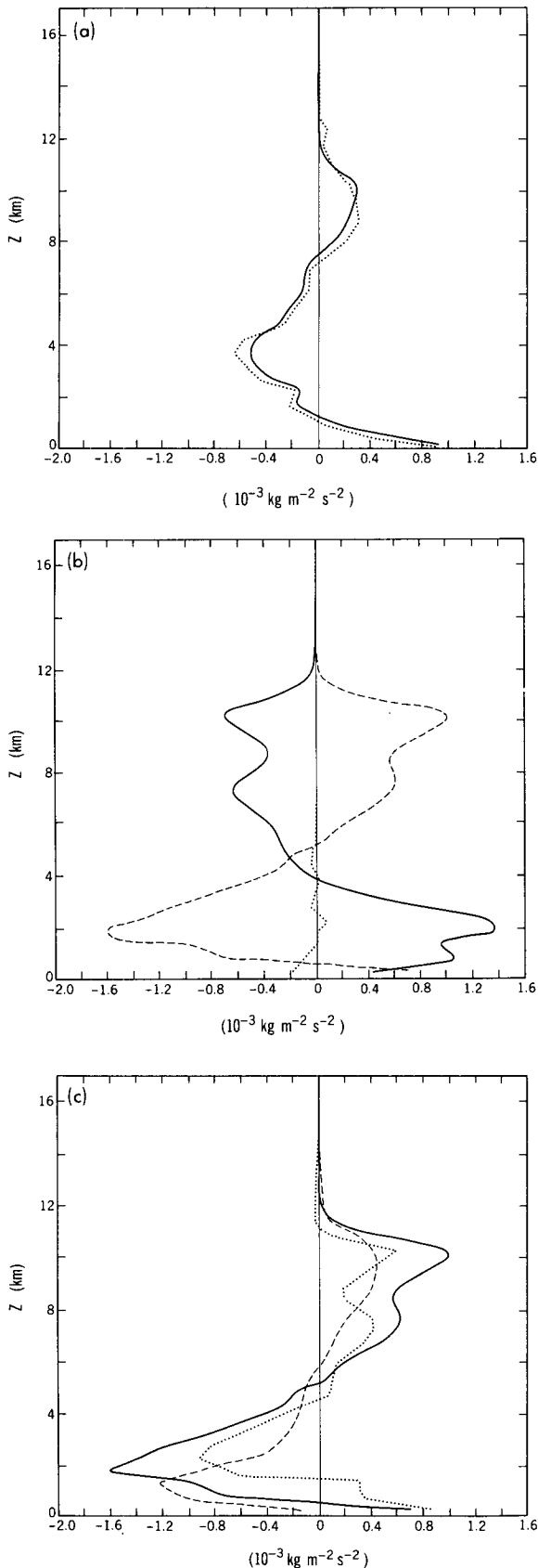
applying the horizontal average and time mean to the momentum equation (2.4'). We obtain

$$\overline{\left\langle \frac{\partial}{\partial t}\rho_0 u_s \right\rangle_s} = -\overline{\left\langle \frac{\partial}{\partial x}[\rho_0(\phi_1 + u_s u_s)] \right\rangle_s}$$

$$- \frac{\partial}{\partial z}[\rho_0 \overline{\langle u_s w \rangle_s}] + \frac{\partial}{\partial z}\overline{\langle \tau_{13} \rangle_s} \quad (4.6)$$

$$\overline{\left\langle \frac{\partial}{\partial t}\rho_0 v_s \right\rangle_s} = -\overline{\left\langle \frac{\partial}{\partial x}(\rho_0 u_s v_s) \right\rangle_s}$$

$$- \frac{\partial}{\partial z}[\rho_0 \overline{\langle v_s w \rangle_s}] + \frac{\partial}{\partial z}\overline{\langle \tau_{23} \rangle_s}. \quad (4.7)$$

Due to periodicity at the lateral boundaries in y, terms involving y derivatives vanish in the horizontal average. Also the terms $\langle \partial \tau_{11}/\partial x \rangle_s$ and $\langle \partial \tau_{21}/\partial x \rangle_s$ in (4.6) and (4.7), respectively, are negligible and have been dropped from these equations.

The vertical variation of the terms in the zonal momentum budget (4.6) is shown in Fig. 10. A comparison between the time tendency term in (4.6) following the squall line and the similar term calculated over the full numerical domain is shown in Fig. 10a. As in Fig. 7a for the zonal momentum flux, these two curves are very similar. The time tendency term in (4.6) is the sum of the three budget terms on the right side of (4.6), which are plotted in Fig. 10b. The Reynolds stress term is seen to be almost negligible. The other two terms tend to compensate each other at nearly all vertical levels, the primary exception being the lowest level at $z = 0.25$ km. Thus, while the squall line is not exactly in a steady state, there is some balance between the two primary budget terms.

At $z = 0.25$ km the two primary budget terms are both positive, giving a significant positive zonal momentum tendency at this level. As in Fig. 8a, where the zonal wind following the squall line has a realistic maximum at this level, we hypothesize that this effect is due to the strong gust front outflow. From Table 1 we note that the speed of the gust front is 1.2 m s^{-1} faster toward the east than the speed of the surface rain. Thus, the area of the flow behind the gust front appears to be increasing with time, which is consistent with a positive zonal momentum tendency.

The only other region where the two primary budget terms tend to complement each other is near and just

FIG. 10. Variation of the zonal momentum budget with height. (a) Net budget following the squall line $\overline{\langle \partial \rho_0 u_s/\partial t \rangle_s}$ (solid curve) versus net budget over full domain $\frac{8}{5}\overline{\langle \partial \rho_0 u_s/\partial t \rangle}$ (dotted curve). (b) Vertical variation of budget terms $- \partial[\rho_0 \overline{\langle u_s w \rangle_s}]/\partial z$ (solid curve), $-\overline{\langle \partial[\rho_0(\phi_1 + u_s u_s)]/\partial x \rangle_s}$ (dashed curve), and $\partial[\overline{\langle \tau_{13} \rangle_s}]/\partial z$ (dotted curve). (c) Vertical variation of $-\langle \partial[\rho_0(\phi_1 + u_s u_s)]/\partial x \rangle_s$ (solid curve), $-\overline{\langle \partial(\rho_0 \phi_1/\partial x \rangle_s}$ (dashed curve) and $-\overline{\langle \partial(\rho_0 u_s u_s)/\partial x \rangle_s}$ (dotted curve).

above $z = 3.75$ km, where the largest negative tendency of zonal momentum is present. A smaller net positive tendency exists at $z = 10.25$ km. As seen in Fig. 10a, these extrema in the time tendency are significantly smaller than the positive value at the surface ($z = 0.25$ km). An important point not to be missed in this discussion is that the time tendency is the sum of all three terms on the right side of (4.6); it is not only the convergence of the vertical zonal momentum flux (solid curve in Fig. 10b). Thus, theoretical arguments based only on the latter term need to be viewed with caution.

In Fig. 10c, the first term on the right in (4.6) has been split into its two components, the horizontal pressure gradient term and the horizontal gradient of the horizontal momentum flux. It is seen that these two terms have somewhat similar vertical variations, but are out of phase. At most levels their net effect is additive so that the combined term in (4.6) is larger than either component. The primary exception is near the surface where the two terms have opposite signs.

The vertical variation of the terms in the meridional momentum budget (4.7) is shown in Fig. 11. As in Fig. 10a, a comparison between the time tendency term in (4.7) following the squall line and the analogous term calculated over the full numerical domain is shown in Fig. 11a. Here significant differences are seen between these two curves, in contrast to Fig. 10a. This

comparison is qualitatively similar to that seen in Fig. 7b where two analogous curves are shown for the vertical meridional momentum flux. Note that due to the relatively smaller terms in the meridional momentum budget, the scale of the abscissa in Fig. 11 has been reduced by a factor of two compared with Fig. 10.

The three budget terms on the right side of (4.7) are plotted in Fig. 11b. Here the Reynolds' stress term makes a significant contribution to the total time tendency below $z = 4.5$ km. Again the two primary terms generally compensate each other so that the net time tendency is small. The oscillatory behavior seen in both Figs. 11a and 11b can be related to the vertical variation of the v-velocity seen in Fig. 8b. Due to the periodicity in y, there is no horizontal pressure gradient term in the meridional momentum budget. The periodicity imposed in the model squall line is an artificial constraint and may limit the validity of the present results compared with observations.

c. The parameterization scheme of Schneider and Lindzen

Schneider and Lindzen (1976, hereafter referred to as SL76) take a horizontal average over the clouds and their environment to obtain the disturbance momentum flux
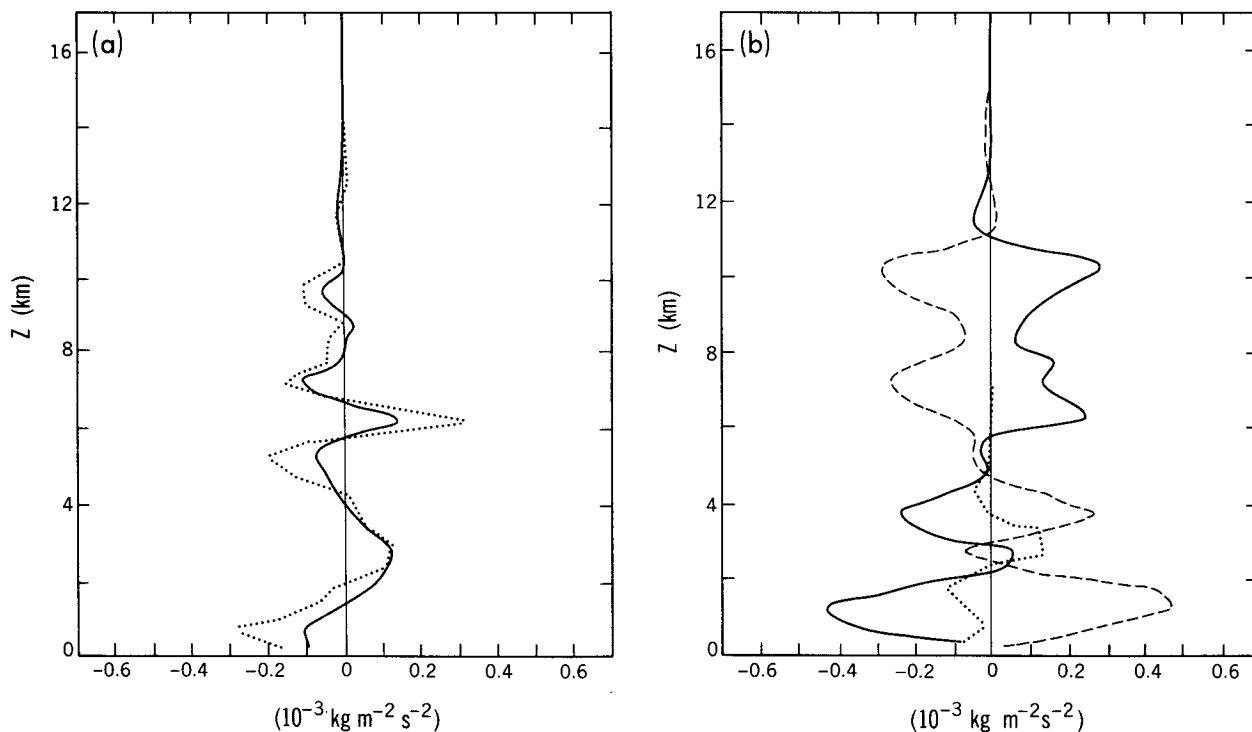

FIG. 11. Variation of the meridional momentum budget with height. (a) Net budget following the squall line $\overline{\langle \partial\rho_0 v_s/\partial t \rangle}_s$ (solid curve) versus net budget over full domain $\frac{8}{5}\overline{\langle \partial\rho_0 v_s/\partial t \rangle}$ (dotted curve). (b) Vertical variation of budget terms $- \partial[\overline{\rho_0\langle v_s w \rangle_s}]/\partial z$ (solid curve), $-\langle \overline{\partial\rho_0 u_s v_s/\partial x} \rangle_s$ (dashed curve), and $\partial\langle \tau_{23} \rangle_s]/\partial z$ (dotted curve). Note change in abscissa scale compared with Fig. 10.
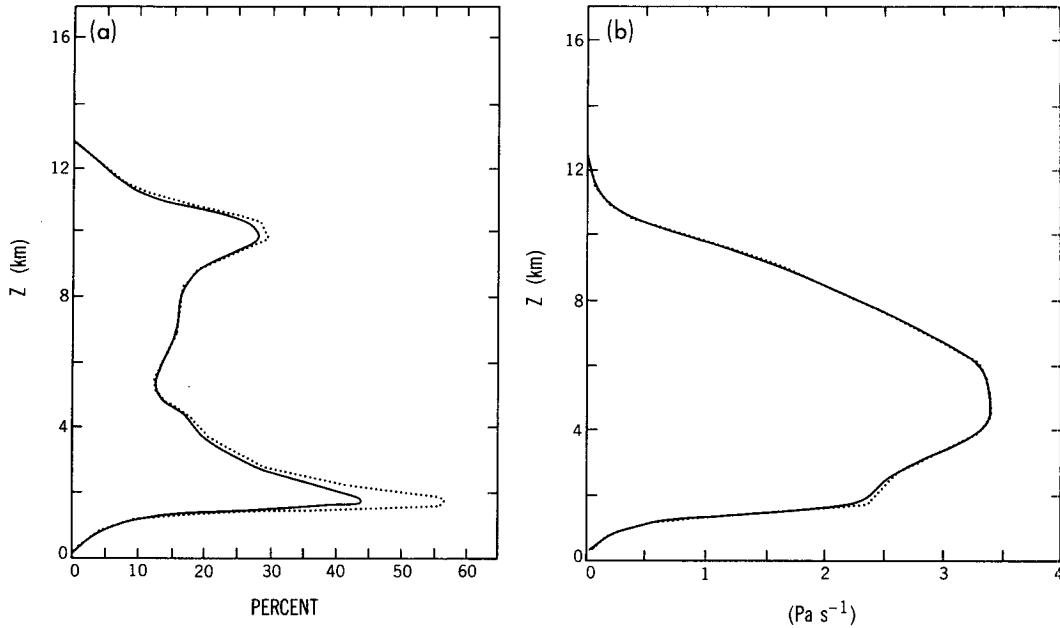
FIG. 12. (a) Time-mean horizontal average cloud fraction CF following the squall line (solid) versus the normalized cloud fraction $8/5$ CF_{tot} calculated over the total numerical domain (dotted curve). (b) Time-mean horizontal average in-cloud upward mass flux $\bar{M}_c$ following the squall line (solid curve) versus the normalized in-cloud upward mass flux $\frac{8}{5}$ $(\bar{M}_c)_{tot}$ calculated over the total numerical domain (dotted curve).

$$-(\rho_0 \langle u'_{si} w' \rangle_s)_{SL} = M_c(\langle u_{si} \rangle_s - (u_{si})_c) \quad (4.8)$$

where M_c is the vertical in-cloud[1] mass flux and $(u_{si})_c$ is the vertically varying horizontal mean u_{si} inside the clouds. Since $(u_{si})_c$ is an unknown function of height, the assumption is made that the net horizontal accelerations of the rising in-cloud parcels are small so that $(u_{si})_c$ can be taken as constant. This constant velocity is set equal to $(u_{si})_{CB}$, which is the horizontal average velocity at cloud base (SL76; Soong and Tao 1984).

The preceding notation indicates that the present coordinate system is following the squall line with the horizontal average $\langle \ \rangle_s$ being taken in the 60-km subdomain as explained in section 4a. Note, that for a given horizontal area, the disturbance vertical momentum flux is the same whether calculated with respect to the fixed earth or the moving squall line.

In the present analysis a time average of (4.8) is taken following the squall line. With $(u_{si})_c$ in (4.8) being set equal to $(u_{si})_{CB}$, we obtain

$$-(\rho_0 \overline{\langle u'_{si} w' \rangle}_s)_{SL} = \bar{M}_c(\overline{\langle u_{si} \rangle}_s - \overline{(u_{si})}_{CB}). \quad (4.9)$$

In this expression it has been assumed that $\overline{\langle u_{si} \rangle}_s$ and $\overline{(u_{si})}_{CB}$ vary slowly with time so that (4.9) can be writ-

ten as a product of time averages. A similar approximation given by (4.4) has been found to be adequate for the present simulation.

There are several assumptions involved in obtaining (4.8) and (4.9). Schneider and Lindzen (1976) state that the main assumption leading to (4.8) is that the fractional area covered by *active* clouds is much smaller than unity. Figure 12a shows the time-mean horizontal-averaged cloud fraction (CF) calculated for the 60-km subdomain moving with the squall line (solid curve). The dotted curve in this figure represents the cloud fraction calculated over the full numerical domain, normalized so that the two curves overlie each other if all the clouds are in the 60-km subdomain following the squall line. These two curves nearly overlie each other at most vertical levels. At 10 km a few cirrus outflow clouds leave the subdomain, but the maximum number of clouds outside the subdomain occurs near the cloud base where low-level inflow into the squall line is occurring. These clouds are found ahead of the squall line. For the squall-line domain the midlevel minimum cloud fraction CF = 13% occurs at 5.5 km. The maximum cloud fraction at 10 km is 28% and that near cloud base (1.75 km) is 44%. These values of CF appear rather large; however, it will be argued in the following that the larger values are made up of primarily inactive clouds.

Figure 12b shows the in-cloud mean upward mass flux $\bar{M}_c$ for the subdomain following the squall line

---

[1] Schneider and Lindzen include the area with "cloud roots" below cloud base in their definition of a cloud. Vertical mass flux below cloud base is not included in the present calculation of M_c.

(solid curve) and the corresponding normalized in-cloud upward mass flux for the full numerical domain (dotted curve). These two curves show definitely that the in-cloud upward mass flux is associated with the moving squall line; only near cloud base is the in-cloud upward mass flux over the total numerical domain slightly larger than for the moving subdomain. Note that the largest values of $\bar{M}_c$ occur in midlevels where values of CF are small. Thus, we conclude that the *active* clouds comprise an area of approximately 15% or less in the moving subdomain for this simulation. If the Schneider and Lindzen calculation is performed in the full numerical domain, the active clouds comprise an area of 10% or less. Their calculation has, in fact, been performed using both domains, and the results are very similar. Thus, it appears that the small but finite values of CF for the active clouds do not interfere with the validity of the Schneider and Lindzen theory.

Another key assumption in obtaining (4.9) is that air entering at cloud base conserves its horizontal momentum until exiting the cloud near cloud top. For this assumption to be valid, the net horizontal pressure forcing on a rising parcel must produce a small net acceleration while the parcel is in the cloud. Schneider and Lindzen indicate that they expect this assumption to be more valid for tropical deep convection, where the wind shear and the resultant pressure drag force are less than for midlatitude convection.

Although the effect of cloud-scale downdrafts appears to be important in mid- and lower cloud levels (Lee 1984; and others), their effect has not been incorporated in this parameterization. Thus, we expect (4.9) to agree better with the simulation data in mid- and upper cloud levels. Another limitation on the validity of (4.8) and (4.9) is that the mean horizontal winds are assumed to be homogeneous throughout the region for which these equations are calculated. For a squall line, however, the values of the horizontal velocities vary significantly from ahead of the line to behind it. In spite of these limitations, we will determine to what degree the calculated perturbation vertical momentum flux $\rho_0\overline{\langle u'_{si}w'\rangle}_s$ agrees with (4.9).

The dynamics of the vertical momentum flux is shown more clearly by calculating the alternative flux $(\rho_0\overline{\langle u'_{si}w'\rangle}_s)_a$ for the simulation. This flux is separated into the two components:

$$(\rho_0\overline{\langle u'_{si}w'\rangle}_s)_a = (\rho_0\overline{\langle u'_{si}w'\rangle}_s)_c + (\rho_0\overline{\langle u'_{si}w'\rangle}_s)_e. \quad (4.10)$$

Following SL76, the first component is the momentum flux associated with the clouds, and the second is associated with the environment of the clouds. For the first component,

$$(\rho_0\overline{\langle u'_{si}w'\rangle}_s)_c = \bar{M}_c\overline{(u_{si})_c}. \quad (4.11a)$$

Since $(\rho_0\overline{\langle u'_{si}w'\rangle}_s)_c$ is the total vertical momentum flux inside the clouds, it follows that $\overline{(u_{si})_c}$ represents the values of $\overline{(u_s)_c}$ and $\overline{(v_s)_c}$, which are required for the equality to hold. If the present simulation follows the parameterization (4.9), then $\overline{(u_s)_c} = \overline{(u_s)}_{CB}$ and $\overline{(v_s)_c} = \overline{(v_s)}_{CB}$, which are the horizontal-average time-mean velocities at cloud base.

The second component in (4.10) is given by

$$\rho_0\overline{\langle u'_{si}w'\rangle}_s)_e = -\bar{M}_c\overline{\langle u_{si}\rangle}_s. \quad (4.11b)$$

Thus, the vertical momentum flux for this component is assumed to be due to the interaction of the compensating downward mass flux in the environment and the mean horizontal flow. This assumption follows the theory SL76.

Since $(\rho_0\overline{\langle u'_{si}w'\rangle})_c$ represents the total vertical momentum flux inside the clouds, any difference between the total vertical flux $\rho_0\overline{\langle u'_{si}w'\rangle}_s$ and the alternative vertical flux $(\rho_0\overline{\langle u'_{si}w'\rangle}_s)_a$ must result from (4.11b) not accurately representing the vertical flux in the environment of the clouds. Figure 13 shows the comparison between $\rho_0\overline{\langle u'_{si}w'\rangle}_s$ and $(\rho_0\overline{\langle u'_{si}w'\rangle}_s)_a$. Above $z = 4.5$ km the curves in Fig. 13a indicate that $\rho_0\overline{\langle u'_{s}w'\rangle}_s$ and $(\rho_0\overline{\langle u'_{s}w'\rangle}_s)_a$ agree well. The data in Fig. 13b show that $\rho_0\overline{\langle v'_{s}w'\rangle}_s$ and $(\rho_0\overline{\langle v'_{s}w'\rangle}_s)_a$ agree well above $z = 3.5$ km. The inference is that (4.11b) is a good approximation for the vertical momentum flux in the environment for mid- and upper levels for this simulation. This is the most important result found from Fig. 13. At lower levels the corresponding fluxes agree poorly, especially the fluxes $\rho_0\overline{\langle u'_{s}w'\rangle}_s$ and $(\rho_0\overline{\langle u'_{s}w'\rangle}_s)_a$. At these lower levels the cloud-scale downdrafts, which are neglected in (4.1b), are important.

The vertical variation of the alternative vertical momentum flux $(\rho_0\overline{\langle u'_{si}w'\rangle}_s)_a$ is compared with the parameterization scheme of Schneider and Lindzen $(\rho_0\overline{\langle u'_{si}w'\rangle}_s)_{SL}$ in Fig. 14. Above $z = 3.5$ km the curves for $(\rho_0\overline{\langle u'_{s}w'\rangle}_s)_a$ and $(\rho_0\overline{\langle u'_{s}w'\rangle}_s)_{SL}$ agree reasonably well, as seen in Fig. 14a. From $z = 3.5$ km down to cloud base $(\rho_0\langle u'_{s}w'\rangle_s)_{SL}$ becomes progressively smaller than $\rho_0\overline{\langle u'_{s}w'\rangle}_s)_a$. Note that $(\rho_0\overline{\langle u'_{s}w'\rangle}_s)_{SL}$ makes an even poorer comparison with the total $\rho_0\overline{\langle u'_{s}w'\rangle}_s$, which is larger than $(\rho_0\overline{\langle u'_{s}w'\rangle}_s)_a$ at lower levels (Fig. 13a).

The values of $\overline{(u_s)_c}$, which are required for (4.11a) to be satisfied, are shown in Fig. 14b. Also shown by the dashed line is $\overline{(u_s)}_{CB}$, which is the value of $\overline{\langle u_s\rangle}_s$ at cloud base in Fig. 8a. For this simulation $\overline{(u_s)}_{CB} = -8.7$ m s^{-1}. It is evident that $\overline{(u_s)_c}$ is not constant with height so that in an average sense $\overline{(u_s)_c}$ is not conserved for parcels moving through the cloud. It can be noted, however, that $\overline{(u_s)_c}$ is within 1 m s^{-1} of the cloud base value between 3.25 and 8.25 km, suggesting that relatively small in-cloud zonal accelerations are present
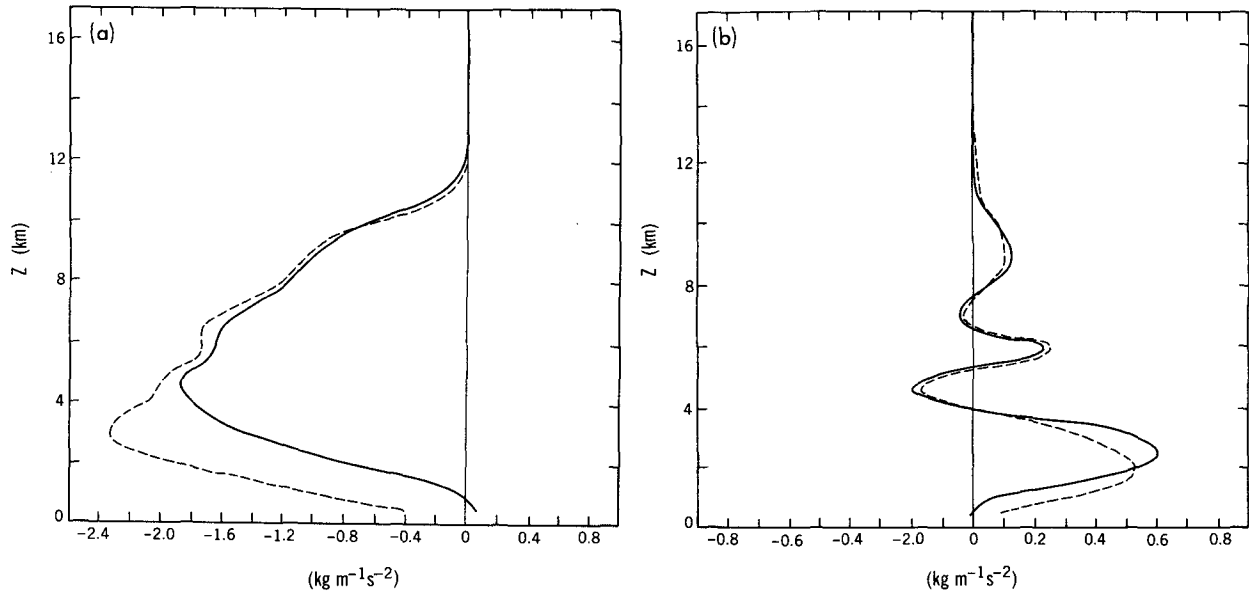
FIG. 13. Comparison of total disturbance momentum flux $\rho_0\langle\overline{u'_{si}w'}\rangle_s$ and $(\rho_0\langle\overline{u'_{si}w'}\rangle_s)_a$ as defined by (4.3) and (4.10). (a) Variation of $(\rho_0\langle\overline{u'_sw'}\rangle_s)_a$ (solid curve) and $\rho_0\langle\overline{u'_sw'}\rangle_s$ (dashed curve) with height. (b) Variation of $(\rho_0\langle\overline{v'_sw'}\rangle_s)_a$ (solid curve) and $\rho_0\langle\overline{v'_sw'}\rangle_s$ (dashed curve) with height.

between these levels. It is interesting to note that the variation of $\overline{(u_s)}_c$ with height for these midlevels is qualitatively similar to the variation of u_s at midlevels inside the cloudy area shown in Fig. 6e.

In Fig. 14c the fluxes $(\rho_0\langle\overline{v'_sw'}\rangle_s)_a$ and $(\rho_0\langle\overline{v'_sw'}\rangle_s)_{SL}$ agree well between 3.0 and 9.5 km. It is equally significant that $\overline{(v_s)}_c$ is virtually independent of height between 2.75 and 9.25 km, as seen in Fig. 14d. Thus, evidently $\overline{(v_s)}_c$ is conserved between these levels, implying no net meridional accelerations. Furthermore, the value of $\overline{(v_s)}_c$ is nearly equal to the cloud base value $\overline{(v_s)}_{CB} = 3.0$ m s^{-1}. The fact that the present data agrees exceptionally well with (4.9) for the vertical meridional momentum flux is not understood; it may be fortuitous. The periodic lateral boundary conditions may be a contributing factor. Although these boundary conditions imply $\langle\overline{\phi_y}\rangle_s \equiv 0$, they do not eliminate the possibility of disturbance pressure gradients acting on in-cloud rising parcels. The symmetry of the present simulation, however, may imply that the mean effect of all such pressure gradients tends toward zero. Thus, the present data for the disturbance meridional momentum flux need to be viewed with caution.

5. Discussion

A detailed analysis has been carried out for a three-dimensional simulation of the 22 May 1976 squall line. We find that the present meso-γ-scale cloud model simulates the leading edge of the squall line reasonably well, but not the long trailing anvil and the underlying

stratiform precipitation shown in the conceptual model of Smull and Houze (1987a). The present model produces significant rain at the ground for approximately 30 min, whereas the observed data of OL80 show precipitation over a period of 2 hours.

It is likely that a part of this discrepancy with observed data is due to the lack of ice bulk cloud physics in the present model. Fovell and Ogura (1988) in their two-dimensional model find more widespread precipitation farther behind the leading edge of the line when the ice phase is included. Additionally, radiative effects of the ice may also maintain and enhance the anvil. Ackerman et al. (1988) showed that anvils may be radiatively destabilized by differential infrared heating over their depth, which can produce upward motion and so increase the size and extent of the anvil.

It is our contention, however, that an accurate simulation of the larger-scale features associated with the squall line cannot be obtained by using only a sounding ahead of the line as input data. Without horizontally varying initial fields and forcing from the larger-scale flow, we must both enhance the moisture profile to account for moisture import into the squall line region and use periodic north–south boundary conditions in order to produce a long-lived squall line. From Fig. 6a we see that the anvil extent in the model is well correlated with the upward motion field, suggesting that a broader upward motion field similar to that seen in Fig. 16 of OL80 and Fig. 1 of Smull and Houze (1987a) might indeed produce a more extensive anvil. Although not proven, we conjecture that convergence forced by
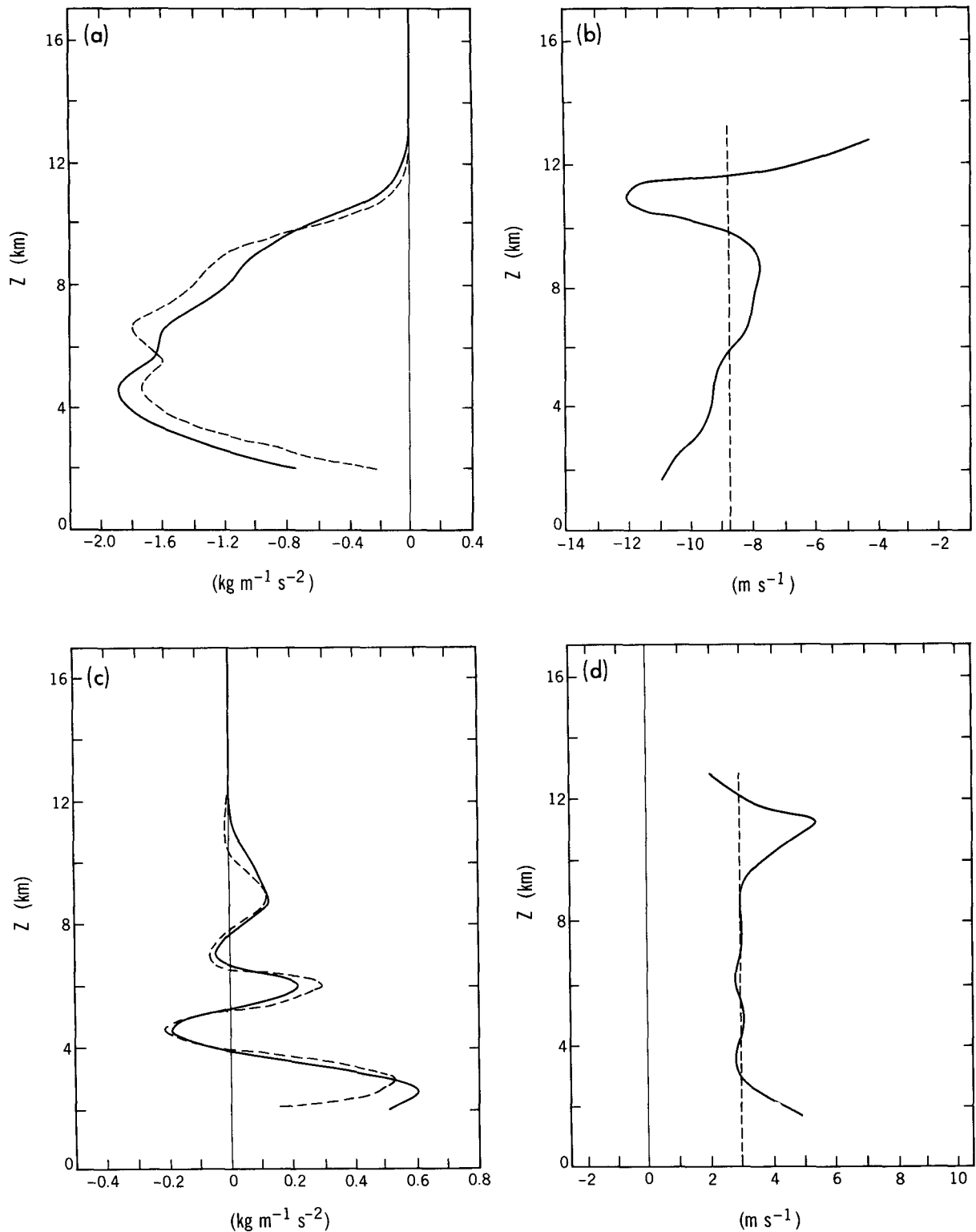
FIG. 14. Comparison of $(\rho_0\overline{\langle u'_{si}w'\rangle_s})_{SL}$ and $\rho_0\overline{\langle u'_{si}w'\rangle_s})_a$. (a) Variation of $(\rho_0\overline{\langle u'w'\rangle_s})_a$ (solid curve) and $(\rho_0\overline{\langle u'w'\rangle_s})_{SL}$ (dashed curve) with height. (b) Variation of $\overline{(u_s)}_c$ with z (solid curve). The dashed line is $\overline{(u_s)}_{CB}$. (c) Variation of $(\rho_0\overline{\langle v'_sw'\rangle_s})_a$ (solid curve) and $(\rho_0\overline{\langle v'_sw'\rangle_s})_{SL}$ (dashed curve) with height. (d) Variation of $\overline{(v_s)}_c$ with z (solid curve). The dashed line is $\overline{(v_s)}_{CB}$.

a combination of convective and larger-scale dynamics is needed to produce such a vertical motion field. Simply including a bulk ice field and its radiative effects are probably insufficient to produce an anvil as extensive as was observed.

Another deficiency of the simulation, which can be attributed to the lack of larger-scale influence, is the general absence of northwest winds following passage of the gust front. Surface observations of OL80 indicate a wind shift from southeast to northwest as the gust front passes. However, the initial sounding taken from Fig. 2 of OL80 does not have northwest winds at any level. Thus, as discussed in section 3, there is no dynamical reason to expect northwest winds at the surface behind the gust front, and they were not present in the simulation, as seen in Fig. 5. Smull and Houze (1987b), however, show three sounding *behind* the squall line, which have a layer of northwest winds at midlevels. Had this information been available to the model, it is possible that a more realistic wind shift following the gust front would have been obtained.

Nevertheless, since the simulation of the convectively active region of the squall line is reasonably good, we are able to analyze and discuss the vertical momentum flux associated with the system, most of which occurs in that region. An important conclusion is that for the component of horizontal momentum normal to the line, the present data for $\rho_0 \langle u_s' w' \rangle_s$ agree with the observational data of LeMone et al. (1984). The data for the component of horizontal momentum parallel to the line appear reasonable, but may be suspect due to the proximity of the lateral boundaries and the periodic conditions applied there.

The time-mean horizontal-averaged momentum budgets have been calculated for $\rho_0 u$ and $\rho_0 v$. Both budgets show a quasi-steady state in which the sum of the terms is typically much less than the magnitude of individual terms in the budgets. The primary exception is near the surface for the $\rho_0 u$-momentum budget where the net time tendency is strongly positive. It is hypothesized that this positive tendency is a result of the gust front moving eastward faster than the precipitation area. For most vertical levels, the convergence of vertical $\rho_0 u$-momentum flux is in a near balance with the sum of the pressure gradient term and the horizontal gradient of the horizontal momentum flux (Fig. 10b). It is not a good approximation to assume that the time tendency term is simply the convergence of the vertical line-normal momentum flux.

The present data agree well with the parameterization scheme of Schneider and Lindzen (1976) when the comparison is limited to the effect of in-cloud vertical momentum flux. However, the total vertical momentum flux, which includes the flux associated with convective-scale downdrafts, is seen to be underestimated by the SL76 parameterization, primarily in low

levels where the downdrafts are significant. The exceptional agreement found for the vertical v-momentum flux may be influenced by the periodic lateral boundary conditions.

REFERENCES

Ackerman, T. P., K.-N. Liou, F. P. J. Valero and L. Pfister, 1988: Heating rates in tropical anvils. *J. Atmos. Sci.*, **45**, 1606–1623.

Bluestein, H. B., and M. H. Jain, 1985: Formation of mesoscale lines of precipitation: Severe squall lines in Oklahoma during the spring. *J. Atmos. Sci.*, **42**, 1711–1732.

Chalon, J. P., G. Jaubert, F. Roux and J. P. Lafore, 1988: The West African squall line observed on 23 June 1981 during COPT81: Mesoscale structure and transports. *J. Atmos. Sci.*, **45**, 2744–2763.

Cho, H.-R., and T. L. Clark, 1981: A numerical investigation of the structure of vorticity fields associated with a deep convective cloud. *Mon. Wea. Rev.*, **109**, 1654–1670.

Clark, T. L., 1979: Numerical simulations with a three-dimensional cloud model: Lateral boundary condition experiments and multicellular severe storm simulations. *J. Atmos. Sci.*, **36**, 2191–2215.

Fovell, R. G., and Y. Ogura, 1988: Numerical simulation of a midlatitude squall line in two dimensions. *J. Atmos. Sci.*, **45**, 3846–3879.

——, and ——, 1989: Effect of vertical wind shear on numerically simulated multicell storm structure. *J. Atmos. Sci.*, **46**, 3144–3176.

Kessler, E., 1969: *On the Distribution and Continuity of Water Substance in Atmospheric Circulations. Meteor. Monogr.*, No. 32, Amer. Meteor. Soc., 84 pp.

Klemp, J. B., and R. B. Wilhelmson, 1978: The simulation of three-dimensional convective storm dynamics. *J. Atmos. Sci.*, **35**, 1070–1096.

Lafore, J.-P., J.-L. Redelsperger and G. Jaubert, 1988: Comparison between a three-dimensional simulation and Doppler radar data of a tropical squall line: Transports of mass, momentum, heat, and moisture. *J. Atmos. Sci.*, **45**, 3483–3500.

Lee, C.-S., 1984: The bulk effects of cumulus momentum transports in tropical cyclones. *J. Atmos. Sci.*, **41**, 590–603.

LeMone, M. A., 1983: Momentum transport by a line of cumulonimbus. *J. Atmos. Sci.*, **40**, 1815–1834.

——, G. M. Barnes and E. J. Zipser, 1984: Momentum flux by lines of cumulonimbus over the tropical oceans. *J. Atmos. Sci.*, **41**, 1914–1932.

Lipps, F. B., and R. S. Hemler, 1980: Another look at the thermodynamic equation for deep convection. *Mon. Wea. Rev.*, **108**, 78–84.

——, and ——, 1982: A scale analysis of deep moist convection and some related numerical calculations. *J. Atmos. Sci.*, **39**, 2192–2210.

——, and ——, 1986: Numerical simulation of deep tropical convection associated with large-scale convergence. *J. Atmos. Sci.*, **43**, 1796–1816.

——, and ——, 1988: Numerical modeling of a line of towering cumulus on Day 226 of GATE. *J. Atmos. Sci.*, **45**, 2428–2444.

Moncrieff, M. W., and M. J. Miller, 1976: The dynamics and simulation of tropical cumulonimbus and squall lines. *Quart. J. Roy. Meteor. Soc.,* **102,** 373–394.

Ogura, Y., and M.-T. Liou, 1980: The structure of a midlatitude squall line: A case study. *J. Atmos. Sci.,* **37,** 553–567.

——, and N. A. Phillips, 1962: Scale analysis of deep and shallow convection in the atmosphere. *J. Atmos. Sci.,* **19,** 173–179.

Orlanski, I., 1976: A simple boundary condition for unbounded hyperbolic flows. *J. Comput. Phys.,* **21,** 251–269.

Redelsperger, J.-L., and J. P. Lafore, 1988: A three-dimensional simulation of a tropical squall line: Convective organization and thermodynamic vertical transport. *J. Atmos. Sci.,* **45,** 1334–1356.

Rotunno, R., J. B. Klemp and M. L. Weisman, 1988: A theory for strong, long-lived squall lines. *J. Atmos. Sci.,* **45,** 463–485.

Schneider, E. K., and R. S. Lindzen, 1976: A discussion of the parameterization of momentum exchange by cumulus convection. *J. Geophys. Res.,* **81,** 3158–3160.

Smull, B. F., and R. A. Houze, Jr., 1985: A midlatitude squall line with a trailing region of stratiform rain: Radar and satellite observations. *Mon. Wea. Rev.,* **113,** 117–133.

——, and ——, 1987a: Dual-Doppler radar analysis of a midlatitude squall line with a trailing region of stratiform rain. *J. Atmos. Sci.,* **44,** 2128–2148.

——, and ——, 1987b: Rear inflow in squall lines with trailing stratiform precipitation. *Mon. Wea. Rev.,* **115,** 2869–2889.

Soong, S.-T., and W.-K. Tao, 1984: A numerical study of the vertical transport of momentum in a tropical rainband. *J. Atmos. Sci.,* **41,** 1049–1061.

Weisman, M. L., and J. B. Klemp, 1982: The dependence of numerically simulated convective storms on vertical wind shear and buoyancy. *Mon. Wea. Rev.,* **110,** 504–520.

——, J. B. Klemp and R. Rotunno, 1988: Structure and evolution of numerically simulated squall lines. *J. Atmos. Sci.,* **45,** 1990–2013.

Yoshizaki, M., and Y. Ogura, 1988: Two- and three-dimensional modeling studies of the Big Thompson storm. *J. Atmos. Sci.,* **45,** 3700–3722.